Frataxin depletion leads to decreased soma size and activation of AMPK metabolic pathway in dorsal root ganglia sensory neurons

Olivier Griso[1,2,3,4], Deepika M. Chellapandi[5], Amélie Weiss[1,2,3,4], Ioannis Manolaras[1,2,3,4], Hélène Puccio[1,2,3,4,5].

[1]Institut de Génétique et de Biologie Moléculaire et Cellulaire (IGBMC), 67404 Illkirch, France; [2]Institut National de la Santé et de la Recherche Médicale (INSERM), U1258, 67404 Illkirch, France; [3]Centre National de la Recherche Scientifique (CNRS), UMR7104, 67404 Illkirch, France; [4]Université de Strasbourg, 67000 Strasbourg, France; [5]Université Claude Bernard Lyon 1, CNRS UMR5261, INSERM U1315, Institut NeuroMyoGène (INMG), Pathophysiology and Genetics of Neuron and Muscle (PGNM), 69008 Lyon, France.

Correspondence: Hélène Puccio, Institut NeuroMyoGène (INMG), Pathophysiology and Genetics of Neuron and Muscle (PGNM), 8 avenue Rockefeller, 69008 Lyon, France
E-mail: helene.puccio@inserm.fr

Abstract

Friedreich's ataxia (FA) is an inherited neurodegenerative disorder caused by frataxin deficiency, leading to mitochondrial dysfunction and impaired iron-sulfur (Fe-S) cluster biogenesis. Proprioceptive dorsal root ganglia (DRG) neurons are among the most vulnerable cell types in FA, yet the mechanisms underlying their selective susceptibility remain unclear. Here, we developed a primary culture model of embryonic mouse DRG neurons with complete frataxin depletion, which faithfully reproduces key biochemical hallmarks of FA, including Fe–S enzyme deficiency, mitochondrial iron dysregulation, and oxidative stress. Despite long-term survival, frataxin-deficient neurons exhibited a marked reduction in soma size, identifying a previously unrecognized growth phenotype. Mechanistically, this defect was mediated by AMP-activated protein kinase (AMPK) hyperactivation and suppression of mTOR signaling in response to mitochondrial dysfunction and redox imbalance. Restoration of frataxin expression, genetic inhibition of AMPK, or treatment with α-lipoic acid (ALA) rescued soma growth, normalize ATP levels and reduce AMPK activation. Our findings uncover AMPK-mTOR dysregulation as a key driver of neuronal growth impairment in FA. This robust neuronal model provides new insights into proprioceptive neuron vulnerability and offers a platform for therapeutic discovery.

Introduction

Friedreich's Ataxia (FA) is an early-onset, progressive neurodegenerative disease characterized by mixed sensory and spinocerebellar ataxia associated to hypertrophic cardiomyopathy and increased incidence of diabetes mellitus[1–3]. In most case, FA is caused by a homozygous GAA trinucleotide repeat expansion within the first intron of the frataxin gene (*FXN*)[4]. This expansion promotes heterochromatin formation and the generation of non-canonical DNA structures[5], leading to transcriptional repression of *FXN* and a consequent reduction in frataxin protein levels to approximately 5-30% of normal [3]. FXN is a mitochondrial protein essential for the biogenesis of iron-sulfur clusters (Fe-S), key cofactors in numerous cellular processes [6]. Accordingly, frataxin deficiency leads to a primary loss of Fe-S synthesis, impairs mitochondrial dysfunction, and perturbs iron metabolism, as observed in patient tissues and a variety of cellular and animal models [7–10]. Increased sensitivity to oxidative stress has also been reported in several models [8,11]. Thus, mitochondrial dysfunction and reactive oxygen species (ROS) accumulation are thought to be central features of the pathophysiology of FA.

The hallmark of sensory ataxia in FA primarily results from degeneration of the large, myelinated proprioceptive neurons (PNs) located in the dorsal root ganglia (DRG), key component of the sensory system responsible for transmitting information about body position and movement[12]. Although traditionally regarded as a neurodegenerative disease, accumulating evidence points to a significant developmental component, particularly in the sensory system. DRG pathology emerges early in the disease course, possibly preceding symptoms onset, and shows limited progression over time. Neuropathological studies of FA patients reveal hypoplasia of both the DRG and spinal cord, and in some cases, failure of dorsal root fibers to properly enter the spinal cord [13,14]. These findings suggest a failure of sensory system development. Nevertheless, postmortem analyses of patients with long disease duration have also identified signs of active neuroinflammation in the DRG, indicative of ongoing degeneration[15]. Taken together, these observations support a model in which both developmental deficit and progressive neurodegeneration contribute to DRG pathology in FA. The selective vulnerability of PNs in FA remains incompletely understood, particularly given the broad tissue expression of frataxin. However, frataxin is developmentally regulated and peaks during critical stages of sensory neuron differentiation and maturation in the mouse embryo[16]. Within the mature DRG, frataxin expression is highest in the PNs, correlating with their susceptibility to disease degeneration[17].

A variety of cellular models have been established to explore the effect of frataxin deficiency in sensory neurons. Primary DRG cultures from adult mice carrying a GAA expansion or from rat with frataxin knockdown recapitulate aspects of FA pathology, including mitochondrial dysfunction, impaired neurite outgrowth, altered growth-cone dynamics, and disrupted calcium signaling[18–20]. More recently, iPSC-derived sensory neurons from FA patients have been shown to exhibit downregulation of transcription factors involved in PN specification and survival, abnormal neurite processes, delayed electrophysiological maturation, and transcriptomic dysregulation affecting cytoskeletal organization, neurite extension, synaptic plasticity, and neurotransmission[21–23]. While these models support the notion of both developmental impairment and neurodegeneration, the molecular pathways underlying these phenotypes remain insufficiently defined. Furthermore, the phenotypes observed in these systems tend to be modest and variable, limiting their utility for mechanistic dissection and high-throughput screening (HTS).

To overcome these limitations, we developed an *in vitro* model of FA based on primary cultures of embryonic mouse DRG sensory neurons carrying a conditional *Fxn* allele[24]. Upon Cre-mediated excision, these cultures exhibit complete frataxin deficiency, enabling longitudinal studies of mitochondrial function, oxidative stress, and cellular morphology. Although more severe than partial deficiency, this model recapitulates key pathological features of FA, including Fe-S deficiency, mitochondrial iron accumulation, altered bioenergetics, and sensitivity to oxidative stress. In the present study, we use this model to investigate the impact of FXN loss on the metabolic and morphological integrity of DRG sensory neurons. We found that frataxin-deficient neurons remain viable for extended periods despite severe mitochondrial dysfunction but display a pronounced reduction in soma size. Mechanistically, we identified overactivation of the AMP-activated protein kinase (AMPK) and suppression of mTOR signaling as central mediators of this growth defect. In addition, we demonstrated that FXN deficiency compromises lipoic acid-dependent enzymatic pathways and that supplementation with alpha-lipoic acid (ALA) restores neuronal growth through both metabolic and antioxidant mechanisms. Collectively, our findings establish a mechanistic link between frataxin depletion, dysregulated metabolic signaling, and impaired neuronal growth, and provide a robust platform for therapeutic screening in FA.

Material & Methods

Establishment of a mouse primary DRG sensory neurons culture, infections and treatments.

Neuronal cultures. Mouse primary DRG sensory neurons were cultures as recently published [24]. 96-well plates were coated with poly-L-lysine (0.1 mg/ml; Merck, P5899), laminin (3.3 ug/ml; ThermoFisher Scientific 23017-015), and Matrigel (1/40 dilution; Corning BV 354277). DRG collected from E13.5 embryos from pregnant mice carrying the conditional allele for the *Fxn* gene (*Fxn*$^{L3/}$L3)[10] and enzymatically digested to dissociate the tissue. Cells (sensory neurons + glial cells) were seeded at a density of 7,500 cells/well and left incubated for 20 minutes (min) at room temperature (RT) before transferring the plates at 37°C, 5% CO_2. The day after, cultures were treated with antimitotic (10 µM Uridine; 9.9 M FUdR) to remove proliferating glial cells from the culture (Fig. 1A, Fig. S1).

Mice were maintained in a pathogen-free animal facility with a 12-hour light/dark cycle and provided with standard rodent chow (D04, SAFE, Villemoisson-sur-Orge, France), water and libitum. All animal procedures were performed in accordance with institutional animal care guidelines and approved by the local ethical committee (APAFIS# 54248-2024102512328818).

Plasmids. Bacterial LplA gene cDNA was cloned from *E. coli* (TOP10 strain) using the following primers: Fwd 5'-CACATTGCGCAAGAAATGCC3' and Rev 5'ATGTCCACATTACGCCTGCT3'). A mitochondrial targeting sequence (MTS) was obtained from mouse *CoxIV*, added 5' of the LplA cDNA fragment, and the entire mtLplA fragment was cloned into a pAAV-CMV vector (Stratagene). The AMPKα1-K56R-HA mutant was generated by overlap extension PCR. Two partially overlapping fragments were amplified independently and subsequently fused to introduce the point mutation.

PCR1 primers: Forward: 5′-attattATCGATATGCGCAGACTCAGTTCCTG-3′; Reverse: 5′-CCGGTTGAGTATCCTCACAG-3′. PCR2 primers: Forward: 5′-attattaagctttcaAGCGTAATCTGGAACATCGTATGGGTACTGTGCAAGAATTTTAATTA GATTTGC-3′; Reverse: 5′-GACATAAAGTGGCTGTGAGG-3′. The two PCR fragments shared a 35-nucleotide overlap, enabling fusion in a secondary PCR reaction. Both fragments were first amplified separately under standard conditions, purified, and then used as templates for the fusion PCR to yield the full-length AMPKα1-K56R-HA construct, which was cloned into a pAAV-CMV vector (Stratagene).

Viral infections. All viral vectors were produced and purified in the IGBMC in-house viral vector production facility (Strasbourg, France), following the helper-free method. For viral infections, AAV were diluted in NB medium [24] at a final concentration of $9x10^9$ vg/ml (unless indicated) and added to neuronal cultures overnight. The next day, AAV containing medium was fully replaced by fresh NB medium. Infections with either AAV9-empty (control) or AAV9-CreGFP (to excise exon 4 from the *Fxn* conditional allele) viruses were performed 3 hours after plating the cells (that is at 0 days in vitro, div). Infections using AAV9-CAG-hFXN-HA[17], AAV9-mtLplA and AAV9-AMPKα1-K56R-HA were performed at 7 div.

Doses of AAV9-CAG-hFXN-HA are as followed and expressed in VG/mL:

D1	5,88E+06	D5	9,00E+08
D2	3,60E+07	D6	4,50E+09
D3	9,20E+07	D7	9,00E+09
D4	1,80E+08		

Cellular treatments. Neuronal cultures were treated starting at 7 div (unless indicated) with either (±)-α-Lipoic acid (ALA; Merck T1395), AICAR (Merck, A9978), N-Acetyl-L-cysteine (Merck A7250), Compound 991 (Selleckchem ex229; S8654) or Rapamycin (Merck R8781). Fresh medium with chemicals was added every 3 to 4 days. In some experiments, cells were cultured either under normal (25 mM glucose) or glycolysis inhibitory (5 mM glucose or 10 mM galactose in glucose-free NB (Gibco A2477501) conditions starting at 7 div.

Immunofluorescence experiments. DRG sensory neurons cultures were fixed for 15 min in 2% PFA diluted in PBSS and stained as described below. Lumbar mouse DRG were harvested from adult mice and fixed for 1h in 4% PFA. To obtain cryosection (8 µm) for immunofluorescence experiments, DRG were embedded in Shandon Cryomatrix resin (ThermoFisher 6769006) and snapfrozen in isopentane chilled on dry ice.

The following staining protocol was used for both sensory neuron cultures and DRG tissue floating sections. First, samples were permeabilized using 0.2% Triton X-100 diluted in PBSS, for 10 min, washed 3 times (5 min each) in PBSS, and blocked for 1 hour (h) with 1% BSA, 5% NGS, 0.1% Tween-20 in PBSS (PBSST). Samples were then incubated overnight at 4°C with the primary antibodies (Table S1) diluted in 1% BSA in PBSST. After 3 more washes in PBSST, secondary antibodies (Table S1) (1/2000) with DAPI (1/1000) were added and incubated for 30 min at RT. For actin staining, Rhodamine Phalloidin (1/2000 dilution,

tebu-bio PHDR1) was added to the secondary antibody solution. Samples were finally washed twice in PBSST and twice in PBSS (5 min each) and mounted using Aqua-Poly/Mount (Polysciences18606) mounting medium.

Electronic microscopy. Sensory neurons cultures were fixed for 15 min in a solution containing 2.5% PFA, 2.5% glutaraldehyde, and 0.1M sodium cacodylate (pH = 7.2). Samples were then processed as previously described [10,25].

Protein extract and Western blots. Sensory neurons were collected and centrifuged at 6000 x g for 1 min. Pellets were resuspended in RIPA Lysis Buffer and incubated on ice for 20 min. After centrifugation for 10 min at 11.000 x g and at 4°C, supernatant was collected, and protein concentration measured by Bradford Assay. Desired quantity of total protein (generally 5µg/sample/gel) was pre-stained for 30 min using QuickStain Protein Labelling Kit (Amersham RPN4000) according to manufacturer's instructions. Proteins were then mixed with loading buffer and boiled for 5 min, loaded on polyacrylamide gels, and separated by electrophoresis. Proteins were then tank-transferred onto a nitrocellulose membrane. After transfer, total protein fluorescence was acquired on an Amersham Imager 600 (GE Healthcare Life Sciences). Membranes were then blocked for 1h in Tris-buffered saline (TBS) containing 5% BSA and Tween-20 (TBST). Membranes were washed 3 times in TBST (10 min each) at RT and incubated with secondary antibodies (1/10.000 to 1/20.000) diluted in TBST for 45 min at RT. Membranes were washed 3 times in TBST (10 min each) and signal was revealed by SuperSignal™ West Femto Maximum Sensitivity Substrate (ThermoFisher 34096) using Amersham Imager 600.

Enzymatic activities. Succinate dehydrogenase (SDH) activity measurements were performed on 10 µg of proteins as previously described [10] on a Cary50 spectrophotometer (Varian SA). One unit of SDH activity is defined as the amount of SDH needed to generate 1.0 µmol of Dichlorophenolindophenol (DCPIP) per min (pH 7.2; 25°C). SDH activity was normalized to total protein content. Pyruvate dehydrogenase (PDH) and lactate dehydrogenase (LDH) activities were measured on 10 µg of proteins using colorimetric kits (Merck MAK183 and MAK066, respectively), following manufacturer's instruction and using Synergy HTX reader (Agilent BioTek).

Seahorse analysis. Mitochondrial respiration was measured using a Seahorse Analyser XFe96 (Agilent) and Seahorse XF Cell Mito Stress Test Kit (Agilent 103015-100). Five thousand sensory neurons were seeded *per* well in compatible 96-well plates (Agilent 101085-004), and Seahorse analysis was performed at 15 div. Protocol was followed as per manufacturer's instructions, with the following optimized concentrations of respiratory chain inhibitors: 2 µM Oligomycin, 0.5 µM FCCP, and 0.5 µM of Rotenone/Antimycin A. Mixing steps (Wave Controller 2.4) were reduced to 20 seconds to prevent detaching of the cells from the bottom of the well.

Survival, soma area, mitochondrial mass, MitoSOX, CellROX and TMRM measurements. Sensory neurons were seeded in black 96-well plates (Greiner 655090) and were stained for 3h (at 37°C, 5% CO_2) with Hoechst 33342 (1 mg/ml; Merck 94403), Mitotracker Green FM (50 nM; ThermoFisher M7514), and/or MitoSOX (2.5 µM; ThermoFisher M36008), or CellROX (5 µM; ThermoFisher C10422) or TMRM (200 nM; Invitrogen I34361) diluted in NB culture medium the day of the analysis at different time points depending on the experiment. To determine the sensitivity to exogeneous oxidative stress, oxidative treatment was performed with 10 µM H_2O_2 incubation for 30 min at 37°C, 5% CO_2 before MitoSOX or CellROX staining. Cells were then washed twice in PBSS (10 min each), fixed in 2% PFA for 15 min (except for TMRM, acquired in live cells), and washed twice with PBSS (10 min each). Fluorescence was acquired on a high content reader (Thermofisher Cellomics Arrayscan XTi) and images were analyzed by the Cellomics HCS Studio software. Each dot indicates average fluorescence from one well in a 96-well plate (about 300 cells/well). Hoechst segmentation was also used to count cells for survival analysis. In addition to labeling nuclei, Hoechst provided enough signal in the soma to allow segmentation and measurement of soma area. Pvalb-positive soma area of Pvalb-Cre mouse (FxnL3/L-; Pvalbtm1(Cre)Arbr/J, [17]) were measured using ImageJ. Signal intensity, and area of each sensory neuron was acquired independently, through cell segmentation.

Mitochondrial iron content. Mitochondrial iron was measured in sensory neurons seeded in black 96-well plates, using the fluorescent non-toxic iron sensor RPA (Axxora SQX-RPA). Sensory neurons were stained with Hoechst 33342 (1 ug/mL; Merck 94403) and 2.5 µM RPA in NB medium for 10 min at 37°C and washed three times in PBSS. Fluorescence was acquired on a high content reader (Thermofisher Cellomics Arrayscan XTi), and images were

analyzed by the Cellomics HCS Studio software. Signal intensity of every cell was acquired independently through cell segmentation.

ATP measurements. ATP levels were measured using a fluorometric kit (Merck MAK190), following manufacturer's instructions. Amount of total protein used was optimized to 10 µg/sample/well.

pH measurements. pH in culture media was indirectly assessed by measuring absorbance of phenol red at 415 nm and 560 nm. Ratiometric analysis 415nm/560nm was calculated to obtain pH [26].

Reverse transcription and real time quantitative PCR (RT-qPCR). Total RNA was extracted from frozen sensory neuron cultures pellets using TRIzol reagent (ThermoFisher 15596026), according to the manufacturer's protocol, and treated with DNAse I (Roche 4716728001). cDNA was generated by reverse transcriptase using the SuperScript IV Kit (Invitrogen 18091050), following the manufacturer's protocol. Quantitative RT-PCR was performed using the SYBR Green I Master mix (Roche 04887352001) on Light Cycler 480 (Roche) with primers listed in Table S3. Gene expression was normalized to GAPDH expression, and then in percent of CT.

Amino acid measurements. Amino acid levels in sensory neurons cultures were measured using LC-MS/MS chromatography (LC-MS/MS Xevo TQS micro; Waters) and the Amino Acid Analysis (AAA) kit (Chromsystems) in collaboration with the lab of Dr. Daniel Brumaru (Hôpital de Hautepierre, Strasbourg). Samples were lysed in a hypotonic buffer (10 mM KH_2PO_4, 2 mM EDTA, pH 7.8) and the measures were performed on according to the manufacturer's protocol. Amino acid levels were normalized to total protein levels.

Statistical analyses. All data are presented as mean ± SD. Statistical analyses were carried out using GraphPad Prism software (La Jolla, USA). Student's t tests were used to compare two groups, one-way ANOVA (Kruskal-Wallis test) was used to compare 3 or more groups. Two-way ANOVA with Geisser Greenhouse Correction was used to compare size combined to genotypes and classes of cell area/time points. A value of $p < 0.05$ was considered as significant. Replicates (n) were considered as biological replicates as they correspond to independent cultures issued from a pool of mouse embryos, independently infected and

independently grown until analysis. Fluorescent and blot images show representative results of several experiments. For cell area and fluorescence experiments performed in 96 well plates, graph dots indicate averaged result from every cell of one well (about 300 cells/well).

Results

FXN-depleted DRG sensory neurons recapitulate FA molecular and cellular features

To investigate the impact of FXN deficiency in a disease-relevant cell type, we previously established an *in vitro* culture model for FA based on mouse primary DRG sensory neurons carrying the conditional *Fxn* allele [24]. The DRG were harvested at embryonic stage E13.5 and after dissociation and seeding, the cells were infected with an AAV9-CreGFP vector (KO) or with an empty AAV vector as a control (CT) (Fig. S1A). To obtain pure neuronal culture, glial cells were removed by treatment with an anti-mitotic agent (Fig. S1B). Infection with the AAV9-CreGFP virus to excise the conditional *Fxn* allele, resulted in the complete depletion of FXN expression levels in the culture after 7 div (Fig. S1C), in accordance with the >95% viral infection efficiency [24]. We performed immunofluorescence detection of several markers of sensory neuron subtypes to determine their relative presence over time in the cultures. Surprisingly, all neurons were positive for NF200 (marker for large myelinated sensory neurons, mechanoreceptive and proprioceptive), for parvalbumin (Aß-LTMRs and proprioceptive neurons), and for TrkC (mechanoreceptive and proprioceptive neurons), and a significant proportion of cells were also positive for the nociceptive specific marker calcitonin gene-related peptide (CGRP) (Fig. S1 D). Moreover, expression of these markers was stable over time (7 to 25 div (Fig. S1 D) and no or little differences between control (CT) and FXN-deficient (KO) cultures could be identified (Fig. S1 D, E).

To characterize the frataxin-depleted sensory neurons, FA-associated phenotypes such as Fe-S biosynthesis deficits, iron metabolism dysregulation, mitochondrial activity and oxidative stress were measured (Fig. 1). Activity of the Fe-S enzyme succinate dehydrogenase (SDH) was already found decreased in KO sensory neurons at 15 div and progressed at 21 div (Fig. 1A). In addition, a substantial decrease in mitochondrial and cytosolic Fe-S cluster containing proteins was observed by western blot at 21 div (Figs. 1B and S2A), in line with previously reported instability of the apo-proteins or complexes in the absence of Fe-S cluster [25,27].

Mitochondrial activity assessment in living cells by Seahorse analysis uncovered a significantly reduced basal respiration rate and a severe reduction of respiratory capacity in KO sensory cells compared to the CT at 15 div (Fig. 1C). In agreement with a metabolic switch [28], frataxin-deficient sensory neurons showed evidences of increased glycolysis with acidification of the culture medium (Fig. S2B) and increased activity of lactate dehydrogenase (Fig. S2C). Mitochondrial mass was found increased in KO cells which was exacerbated by inhibiting glycolysis using restrictive carbon sources culture conditions (Fig.

1D). Accordingly, several mitochondrial proteins as well as transcriptional factors involved in mitochondrial biogenesis were found to be increased at the translational levels (Fig. S2D). At the ultrastructural level, KO cells contained giant mitochondria with abnormal structures including collapsed cristae (Fig. 1E).

A direct consequence of Fe-S deficit is the dysregulation of iron metabolism through the Fe-S-dependent activation of the Iron Responsive Element (IRE)-binding Protein IRP1 [30]. An increase of transferrin receptor 1 (TFR1) and a decrease of ferritin light chain (FRTL) was observed in KO cells at 21 div (Fig. 1F), consistent with an activation of IRP1. Increased mitochondrial iron content is another hallmark of the FA disease. Mitochondrial iron content was measured using the fluorescent mitochondrial iron indicator RPA, which signal depends on labile iron content [31]. RPA signal was found to be decreased in the KO sensory neurons at 30 div compared to CT sensory neurons, indicating that labile mitochondrial iron content was increased (Fig. 1G).

Mitochondrial electron transport chain dysfunction is commonly associated with elevated production of reactive oxygen species (ROS)[32]. Numerous FA models present an increased sensitivity to oxidative stress[11]. To assess mitochondrial oxidative stress, we used the mitochondrial-specific fluorescent probe MitoSOX. At early time point (15 div), KO sensory neurons displayed an increase in sensitivity to exogenous oxidative stress compared to CT, despite no observable difference at the basal mitochondrial ROS levels (Fig. 1H). At later stages (21 and 30 div), KO sensory neurons exhibited an increase in endogenous mitochondrial oxidative stress relative to CT neurons (Fig. 1H). In contrast, measurements using the cytosolic ROS probe CellROX at 30 div revealed no increase in cytosolic oxidative stress under basal condition and in the presence of exogenous stress in KO sensory neurons compared to CT (Fig. 1I).

Altogether, these findings demonstrate that the model faithfully recapitulates several key biochemical and cellular pathological features of FA, supporting its relevance for exploring new pathways impacted by frataxin deficiency in sensory neurons.

Frataxin depletion impairs soma size without affecting the survival of sensory neurons

To assess whether frataxin deficiency leads to increased cell death, neuronal survival was evaluated at multiple time points of the culture. Notably, no significant difference in cell number was observed between KO and CT sensory neurons, even at the latest culture stages (30 div) (Fig. 2A). Furthermore, KO neuron viability remained unaffected under glycolysis-inhibiting conditions (Fig. S3). In contrast, a significant difference in soma growth dynamics

between KO and CT sensory neurons was observed. From 7 to 15 div, KO and CT sensory neurons exhibited comparable soma growth (Fig. 2B). While CT soma continued to grow until 21 div, KO soma size plateaued, and subsequently declined slightly by 30 div (Fig. 2B). Quantitatively, KO somas were 1.3-fold smaller than CT at 21 div, and this difference increased to 1.5-fold by 30 div (Fig. 2B). This reduction was confirmed by 3D imaging, which showed a global decrease in KO neuron soma volume compared to CT (Fig 2C). Analysis at the single-cell level revealed a reduced proportion of large soma size neurons in the KO population (Fig. 2D). Since total cell number remains unchanged, these results suggest a global shift in cell size distribution rather than selective loss of large neurons.

Soma size is rescued by frataxin in a dose-dependent manner

To assess whether the KO phenotype could be rescued in a frataxin dose-dependent level, DRG neurons were transduced with increasing doses of an AAV vector encoding HA-tagged human frataxin (AAV9-CAG-hFXN-HA [17]). Anti-HA immunostaining confirmed the dose-dependent transgene expression (Fig. S4). Interestingly, several hallmarks of the FA-phenotype, including Fe-S deficit (assessed indirectly via protein stability; Fig. 3A), mitochondrial oxidative stress (Fig. 3B), and mitochondrial membrane potential impairment (Fig. 3C), were progressively corrected as frataxin expression increased. Importantly, increasing frataxin levels also restored soma size in KO neurons in a dose-dependent manner (Fig. 3D).

Lipoic acid-dependent pathways are impaired in frataxin-deficient neurons

As lipoic acid (LA) synthesis depends on the Fe-S cluster-dependent enzyme lipoic acid synthase (LIAS), we next evaluated protein lipoylation status in KO neurons. Quantitative analysis revealed a pronounced decrease in LA conjugation to both PDH and α-ketoglutarate dehydrogenase (KGDH), two key enzymes of the Krebs cycle (Fig. 4A). Importantly, PDH E2 subunit (PDC-E2) protein levels remained unchanged, suggesting that the reduction in lipoylation reflects functional impairment of LIAS activity. Consistent with this, LIAS protein levels were significantly reduced in KO sensory neurons (Fig. 4A), likely secondary to destabilization resulting from defective Fe-S cluster biogenesis. A significant reduction (~ 2.6-fold) in pyruvate dehydrogenase (PDH) activity, which requires covalent attachment of LA to PDC-E2, was detected in KO sensory neurons, indicating compromised mitochondrial metabolism (Fig. 4B).

Since LA is also a required cofactor for mitochondrial degradation pathways of glycine, lysine, and branched-chain amino acids (BCAAs), we investigated the metabolic consequences of impaired LA-dependent enzyme function. Elevated levels of glycine and BCAAs were detected in KO neurons at 30 div (Fig. 4C), consistent with defective amino acid catabolism due to insufficient lipoylation of dehydrogenase complexes.

To restore LA-dependent enzyme activity in KO neurons, we expressed of Lipoate ligase A (LplA), a bacterial enzyme from the salvage pathway capable of attaching exogenous LA to target proteins, a function absent in mammalian systems, which rely exclusively on *de novo* LA synthesis [33]. For mitochondria targeting, LplA was fused to the human COXV mitochondrial targeting sequence and delivered via AAV9-mediated transduction (mtLplA). Immunofluorescence confirmed efficient mitochondrial localization of mtLplA (Fig. S5A). Expression of mtLplA partially restored LA loading to PDH and KGDH in the absence of exogenous LA, and fully restored lipoylation upon supplementation with ≥ 10 μM α-lipoic acid (ALA) (Fig. S5B). Correspondingly, PDH enzymatic activity was fully rescued under these conditions (Fig. S5C).

Interestingly, while mtLplA expression restored biochemical defects of LA loading and PDH activity, it failed to normalize soma size phenotype (Fig. S5D). Phenotypic rescue required high-dose ALA supplementation, which induced a dose-dependent increase in soma size and shifted the KO soma size distribution toward larger neurons (Fig. S5E). Although mtLplA expression increased the proportion of large neurons, ALA, either alone or combined with mtLplA, resulted in a broader rescue across the neuronal population. These observations suggest that ALA may have additional lipoylated proteins-independent actions, possibly related to its antioxidant properties, that contribute to the restoration of neuronal soma size.

The AMPK pathway is activated in frataxin-deficient neurons

The AMP-activated protein kinase (AMPK) signaling pathway plays a key role in regulating cell growth, metabolism and autophagy [34]. AMPK senses cellular energy status by responding to fluctuations in cellular ATP/AMP ratio. Given the strong decrease in mitochondrial function resulting in low ATP levels (Fig. 5A), we hypothesized that AMPK pathway could contribute to the growth defects observed in KO neurons. Western blot analysis revealed a clear activation of the AMPK pathway at 21 div in KO sensory neurons (Fig. 5B). Specifically, the phospho-AMPKα-Thr172 activation mark was increased by 1.7-fold relative to controls (Fig 5B). In parallel, phosphorylation of several downstream AMPK targets, including ACC, ULK1 and Raptor, were significantly increased in KO neurons (Fig.

5B). Notably, the phosphorylation of ULK1, an autophagy regulator, at Ser555 was increased by 2.4-fold (Fig. 5B), accompanied by elevated phosphorylation of its downstream target Beclin-1 at Ser15 (Fig. S6A).

AMPK is known to inhibit cell growth partly through suppression of the mammalian target of rapamycin complex 1 (mTORC1) pathway [35]. mTOR controls cell growth by promoting anabolic processes, such as protein, lipid and nucleotide synthesis, and suppressing catabolic processes, such as autophagy [35]. AMPK directly phosphorylates Raptor, a regulatory associated protein of mTOR, thereby blocking mTORC1 activity[34]. Consistent with this, phosphorylation of Raptor at Ser792 was increased by 1.7-fold in the KO neurons (Fig. 5B). Furthermore, phosphorylation of mTOR downstream target P70S6K was significantly decreased on several residues (Fig. 5C), indicating inhibition of the mTOR/S6K axis. Interestingly, pharmacological activation of the AMPK pathway with AICAR or Compound 991 treatments reduced soma size in CT sensory neurons (Fig. S6B-D). Similarly, pharmacological inhibition of mTOR pathway using Rapamycin also led to decrease soma size in CT sensory neurons (83 ± 2%) (Fig S6B, S6E). Restoration of frataxin expression in KO neurons progressively normalized both AMPK activation and mTOR pathways inhibition (Fig. S7A).

To directly test whether AMPK activation drives soma size reduction, we inhibited endogenous AMPK activity by overexpressing a dominant-negative AMPKα mutant ($AMPK\alpha^{K56R}$). This approach effectively suppressed AMPK activation, as shown by reduced phosphorylation of AMPKα at Thr172 and decrease phosphorylation of its downstream targets ACC and Raptor (Fig. 5D). Importantly, inhibition of AMPK by $AMPK\alpha^{K56R}$ led to a significant increase in soma size in KO neurons, restoring it to control levels (Fig. 5E). These finding indicate that AMPK activation directly contributes to the soma size phenotype observed in frataxin-deficient neurons.

Antioxidant properties of ALA contribute to phenotypic rescue and prevents AMPK activation in frataxin-deficient neurons

As previously seen, treatment with exogenous LA in the form of ALA partially rescued soma size defects in KO neurons in a dose-dependent manner (Fig. 6A). ALA treatment also improved protein lipoylation, as evidence by a partial restoration of LA conjugation to PDC-E2 (13 ± 2% increase; Fig. S8A). However, ALA had minimal impact on glycine and BCAA levels, although a trend toward normalization was observed (Fig. S8B). ALA treatment significantly reduced mitochondrial oxidative stress in the KO neurons (Fig

6B). The dose-dependent rescue of soma size by ALA prompted us to examine whether this effect might be mediated via AMPK signalling. Phosphorylation of AMPKα at Thr172, a key marker of AMPK activation, was strongly decreased following ALA treatment in KO neurons (Fig 6C). In parallel, phosphorylation of downstream AMPK targets, including ULK1, was also significantly reduced (Fig 6C), indicating suppression of AMPK activity. Given ALA's role in improving mitochondrial function and reducing oxidative stress, we could hypothesize that restored mitochondrial activity may contribute to AMPK downregulation via improved cellular energy status. Consistent with this, ATP levels in KO neurons were significantly restored following ALA treatment (Fig 6D), supporting the notion that ALA might suppress AMPK activation through the restoration of cellular energy balance.

Discussion

In this study, we established a novel primary neuronal model of FA based on mouse DRG sensory neurons with complete FXN depletion. This model faithfully recapitulates key hallmarks of FA, including an early and progressive loss of Fe-S proteins, likely due to impaired Fe-S cluster biogenesis, dysregulated iron metabolism with mitochondrial iron accumulation, and severe mitochondrial dysfunction characterized by decreased mitochondrial oxidative respiration leading to energy deficit, increased mitochondrial mass, and oxidative stress. These phenotypes are consistent with those observed in other FA-relevant cell types such as cardiomyocytes [10,36,37].

Importantly, our data support a model in which full FXN depletion first induces a deficit of Fe-S synthesis, subsequently triggering downstream consequences such as iron dysregulation, mitochondrial proliferation, and redox imbalance. Endogenous oxidative stress was detected at later time points and localized to mitochondria, whereas cytosolic ROS remained unchanged, suggesting a compartment-specific origin of redox perturbation. These observations are in line with findings from DRG sensory neurons from a GAA-based FA mouse model [38].

Mitochondrial mass was increased in FXN-deficient neurons. Since this was not accompanied by improved function, we interpret it as a compensatory response to bioenergetic stress or as a result of impaired mitophagic clearance of damaged organelles. Although mitophagy flux was not directly evaluated, the presence of abnormally enlarged mitochondria with collapsed cristae strongly suggests impaired mitochondrial quality control, a hypothesis that warrants further investigation. Notably, similar mitochondrial abnormalities

were also observed in other neuronal models, including two conditional neuronal mouse models [17,39].

Interestingly, despite pronounced mitochondrial dysfunction, FXN-deficient DRG neurons remained viable for several weeks *in vitro*, even under glucose-restrictive conditions. This metabolic resilience contrasts with the rapid death of dividing cells following FXN loss [40,41], likely due to the critical dependence of cell division and DNA replication on Fe-S proteins essential for these processes [42,43]. These findings are consistent with observations from the *Pvalb* conditional knockout mouse model, in which proprioceptive neurons survived for several weeks complete FXN depletion *in vivo* [17]. This suggests that, although functionally compromised, sensory neurons retain sufficient plasticity to withstand FXN loss over extended periods, providing a potential therapeutic window before irreversible degeneration occurs, as evidenced by full post-symptomatic rescue observed in gene therapy studies [17,25].

A novel phenotype uncovered in our model is a clear defect in soma growth of FXN-deficient neurons. KO neurons failed to achieve normal soma growth and exhibited a progressive reduction in soma size not associated with increased cell death. Interestingly, re-expression of human frataxin rescued soma size in a dose-dependent manner, strongly indicating that the growth deficit is a direct and frataxin-specific phenotype. To our knowledge, this is the first report of a frataxin-dependent regulation of neuronal soma size in DRG neurons. Given that proprioceptive neurons are among the largest DRG subtypes and have extensive metabolic demands, failure to reach an appropriate soma size during development could impair their function or connectivity. It is possible that insufficient frataxin during key developmental windows limits neuronal maturation and growth, thus predisposing these cells to functional failure and eventual degeneration.

FXN-deficient neurons exhibited substantial disruption of lipoic acid (LA)-dependent pathways. Lipoylation of both PDH and KDGH was impaired. Since LA biosynthesis depends on the Fe-S enzyme lipoid acid synthase (LIAS), these findings are consistent with compromised LIAS activity secondary to Fe-S depletion. Protein levels of LIAS were also reduced, likely due to destabilization of the apoenzyme. Consequently, key metabolic pathways relying on lipoylated enzymes, including the Krebs cycle and the mitochondrial degradation of glycine and branched amino acids (BCAAs), were affected with PDH activity significantly reduced and elevated levels of glycine and BCAAs in FXN-deficient neurons. To bypass the endogenous LA synthesis defect, we expressed a mitochondria-targeted version of the bacterial enzyme lipoate ligase A (mtLplA), which salvaging exogenous LA by attaching it to recipient proteins. While mtLplA expression restored PDH and KGDH

lipoylation and PDH activity, it failed to rescue the soma size defect. In contrast, high-dose α-lipoic acid ALA supplementation induced a robust, dose-dependent rescue of soma size, both alone or in combination with mtLplA. Considering that ALA alone does not rescue PDH activity, these findings suggests that ALA exerts effects beyond its role as a cofactor, likely due to its antioxidant properties and impact on cellular signaling.

Mechanistically, we identified AMP-activated protein kinase (AMPK) as a central signaling hub activated in FXN-deficient neurons. FXN loss led to severe mitochondrial dysfunction, reflected by reduced respiratory activity and ATP levels, alongside elevated mitochondrial oxidative stress. This bioenergetic and redox imbalance provides two synergistic signals known to activate AMPK: a high AMP/ATP ratio and accumulation of reactive oxygen and nitrogen species (ROS/RNS). Consistently, we observed increase AMPK phosphorylation at Thr172, along with enhanced phosphorylation of its downstream targets, including ACC, ULK1, and Raptor. This activation leads to the downregulation of mTOR signaling, as evidenced by increased Raptor phosphorylation and reduced phosphorylation of P70S6K, a key mTOR effector. Since mTOR governs anabolic processes such as protein and lipid synthesis and cell growth, its inhibition likely underlies the observed reduction in neuronal soma size. Supporting this, pharmacological AMPK activation or mTOR inhibition mimicked the soma size reduction in control neurons, while genetic inhibition of AMPK using a dominant-negative AMPKα mutant restored soma size in FXN-deficient neurons. These findings establish AMPK activation as both necessary and sufficient to drive the growth deficit.

Although we cannot fully disentangle the relative contributions of energy depletion and oxidative stress to AMPK activation in this model, both appear to play a role. Beyond sensing ATP levels, AMPK is known to respond to redox signals [44], and ROS/RNS have been shown to activate AMPK and promote compensatory metabolic adaptations such as glycolysis and mitochondrial biogenesis, respectively [45–47]. Accordingly, the frataxin-deficient neurons exhibited signs of increased mitochondrial content and glycolytic activity, both hallmarks of AMPK-driven metabolic reprogramming. Moreover, AMPK activation can induce expression of antioxidant response genes, suggesting it may serve as a broader integrator of mitochondrial stress, maintaining cellular homeostasis and promoting cell survival under conditions of stress [48–51].

Together, these findings support a model in which frataxin depletion triggers mitochondrial dysfunction, leading to both ATP depletion and oxidative stress. These stressors converge on AMPK, which in turn inhibits mTOR signaling, thereby impairing

neuronal growth. The fact that AMPK activation is reversed by FXN re-expression further reinforces the link between frataxin status and AMPK activation. Ultimately, our data position AMPK-mTOR dysregulation as a key downstream consequence of frataxin deficiency and a mechanistic driver of the soma size phenotype in DRG neurons.

Interestingly, ALA treatment alone decreased AMPK activation, as shown by reduced phosphorylation of AMPKα and its downstream targets. While ALA is traditionally considered a potent scavenger of ROS, our data indicate that its therapeutic action may also arise from restoring mitochondrial function and intracellular ATP levels, thereby indirectly mitigating AMPK hyperactivation. In support of this, ALA was associated with improved mitochondrial energy output, as reflected by reduced mitochondrial oxidative stress and enhanced intracellular ATP levels. Our findings are consistent with previous reports showing that ALA suppresses AMPK activation in human muscles cells [52] and human neuroblastoma cell line [53], likely via indirect effects on metabolic equilibrium rather than through a direct inhibition of the kinase. In our model, we propose that ALA exerts its beneficial effects primarily by enhancing mitochondrial ATP production and reducing ROS, which leads to reduced AMPK activation, normalizes mTOR signaling, and promotes neuronal growth.

Our work establishes a reliable and pathophysiologically relevant model of FXN-deficient sensory neurons, demonstrating that frataxin loss disrupts mitochondrial function, redox homeostasis, metabolic signaling, and neuronal morphology. It uncovers a previously unrecognized phenotype of soma size reduction and links this to AMPK–mTOR signaling dysregulation. The model's strengths lie in its reproducibility, scalability, and clear phenotype dynamics between control and KO neurons. Its compatibility with medium-throughput systems, such as 96-well plates [24], makes it ideally suited for phenotype-based drug screening, particularly for identifying molecules that can bypass or substitute frataxin activity or modulate AMPK-mTOR signaling. However, the model has limitations. First, sensory neuron differentiation is suboptimal under current culture conditions. Future refinements, such as co-culture with glia or modified trophic support could enhance neuronal maturation and subtype specificity. Second, the use of complete frataxin knockout accelerates disease phenotype but does not fully recapitulate the partial FXN depletion seen in all FA patients. Human iPSC-derived DRG neuron models carrying GAA expansions [54] offer a valuable complementary system for translational validation.

In summary, this study defines a comprehensive cellular framework for understanding frataxin deficiency in sensory neurons. It identifies AMPK-mTOR signaling as a key effector of neuronal soma growth defects and establishes ALA as a candidate therapeutic agent

capable of restoring bioenergetics and redox balance. These findings contribute to our understanding of proprioceptive neuron vulnerability in FA and pave the way for novel therapeutic approaches that target downstream metabolic pathways in addition to frataxin replacement.

Acknowledgments

We thank Anne Maglott-Roth, Laurence Reutenauer, Nadège Diedhiou, Aurélie Eisenmann, Valentine Mosbach and Alain Martelli for technical assistance and discussions. We thank Nadia Messaddeq from the IGBMC imaging platform for EM analysis and Pascale Koebbel (IGBMC molecular biology platform) for vector production. This work was supported by the US Friedreich Ataxia Research Alliance (to H.P.), the Association Franc aise pour l'Ataxie de Friedreich (to H.P. and O.G.) and the Fondation pour la Recherche Médicale (FRM) grant number ECO20160736060 (to O.G.) and FRM grant number FDT202304016821 (to D.M.C). This study was supported by the grant ANR-10-LABX-0030- INRT, a French State fund managed by the Agence Nationale de la Recherche under the frame program Investissement d'Avenir ANR-10-IDEX-0002-02.

Author contributions

Conceptualization, O.G., H.P.; Methodology, O.G., D.M.C., H.P.; Investigation, O.G., D.M.C., A.W., I.M.; Writing O.G., D.M.C., H.P.; Funding Acquisition, O.G., D.M.C., H.P.; Supervision, H.P.

References

1. Delatycki, M.B., and Corben, L.A. (2012). Clinical Features of Friedreich Ataxia. J Child Neurol *27*, 1133–1137. https://doi.org/10.1177/0883073812448230.
2. Harding, A.E. (1981). Friedreich's ataxia: a clinical and genetic study of 90 families with an analysis of early diagnostic criteria and intrafamilial clustering of clinical features. Brain *104*, 589–620.
3. Pandolfo, M. (2009). Friedreich ataxia: The clinical picture. J Neurol *256*, 3–8. https://doi.org/10.1007/s00415-009-1002-3.
4. Campuzano, V., Montermini, L., Moltò, M.D., Pianese, L., Cossée, M., Cavalcanti, F., Monros, E., Rodius, F., Duclos, F., Monticelli, A., et al. (1996). Friedreich's Ataxia: Autosomal Recessive Disease Caused by an Intronic GAA Triplet Repeat Expansion. Science *271*, 1423–1427. https://doi.org/10.1126/science.271.5254.1423.
5. Gottesfeld, J.M. (2019). Molecular Mechanisms and Therapeutics for the GAA·TTC Expansion Disease Friedreich Ataxia. Neurotherapeutics *16*, 1032–1049. https://doi.org/10.1007/s13311-019-00764-x.
6. Lill, R. (2009). Function and biogenesis of iron–sulphur proteins. Nature *460*, 831–

838. https://doi.org/10.1038/nature08301.
7. Martelli, A., Friedman, L.S., Reutenauer, L., Messaddeq, N., Perlman, S.L., Lynch, D.R., Fedosov, K., Schulz, J.B., Pandolfo, M., and Puccio, H. (2012). Clinical data and characterization of the liver conditional mouse model exclude neoplasia as a non-neurological manifestation associated with Friedreich's ataxia. Dis Model Mech *5*, 860–869. https://doi.org/10.1242/dmm.009829.
8. Martelli, A., Napierala, M., and Puccio, H. (2012). Understanding the genetic and molecular pathogenesis of Friedreich's ataxia through animal and cellular models. Dis Model Mech *5*, 165–176. https://doi.org/10.1242/dmm.008706.
9. Perdomini, M., Hick, A., Puccio, H., and Pook, M.A. (2013). Animal and cellular models of Friedreich ataxia. J. Neurochem. *126 Suppl 1*, 65–79. https://doi.org/10.1111/jnc.12219.
10. Puccio, H., Simon, D., Cossée, M., Criqui-Filipe, P., Tiziano, F., Melki, J., Hindelang, C., Matyas, R., Rustin, P., and Koenig, M. (2001). Mouse models for Friedreich ataxia exhibit cardiomyopathy, sensory nerve defect and Fe-S enzyme deficiency followed by intramitochondrial iron deposits. Nat Genet *27*, 181–186. https://doi.org/10.1038/84818.
11. Delatycki, M.B., and Bidichandani, S.I. (2019). Friedreich ataxia- pathogenesis and implications for therapies. Neurobiol. Dis. *132*, 104606. https://doi.org/10.1016/j.nbd.2019.104606.
12. Emery, E.C., and Ernfors, P. (2020). Dorsal Root Ganglion Neuron Types and Their Functional Specialization. In The Oxford Handbook of the Neurobiology of Pain, J. N. Wood, ed. (Oxford University Press), p. 0. https://doi.org/10.1093/oxfordhb/9780190860509.013.4.
13. Koeppen, A.H., Becker, A.B., Qian, J., and Feustel, P.J. (2017). Friedreich Ataxia: Hypoplasia of Spinal Cord and Dorsal Root Ganglia. J. Neuropathol. Exp. Neurol. *76*, 101–108. https://doi.org/10.1093/jnen/nlw111.
14. Koeppen, A.H., Becker, A.B., Qian, J., Gelman, B.B., and Mazurkiewicz, J.E. (2017). Friedreich Ataxia: Developmental Failure of the Dorsal Root Entry Zone. J Neuropathol Exp Neurol *76*, 969–977. https://doi.org/10.1093/jnen/nlx087.
15. Koeppen, A.H., Ramirez, R.L., Becker, A.B., and Mazurkiewicz, J.E. (2016). Dorsal root ganglia in Friedreich ataxia: satellite cell proliferation and inflammation. Acta Neuropathol Commun *4*, 46. https://doi.org/10.1186/s40478-016-0288-5.
16. Jiralerspong, S., Liu, Y., Montermini, L., Stifani, S., and Pandolfo, M. (1997). Frataxin shows developmentally regulated tissue-specific expression in the mouse embryo. Neurobiol Dis *4*, 103–113. https://doi.org/10.1006/nbdi.1997.0139.
17. Piguet, F., Montigny, C. de, Vaucamps, N., Reutenauer, L., Eisenmann, A., and Puccio, H. (2018). Rapid and Complete Reversal of Sensory Ataxia by Gene Therapy in a Novel Model of Friedreich Ataxia. Molecular Therapy *0*. https://doi.org/10.1016/j.ymthe.2018.05.006.
18. Sanz-Alcázar, A., Britti, E., Delaspre, F., Medina-Carbonero, M., Pazos-Gil, M., Tamarit, J., Ros, J., and Cabiscol, E. (2023). Mitochondrial impairment, decreased sirtuin activity and protein acetylation in dorsal root ganglia in Friedreich Ataxia models. Cell. Mol. Life Sci. *81*, 12. https://doi.org/10.1007/s00018-023-05064-4.
19. Sanz-Alcázar, A., Portillo-Carrasquer, M., Delaspre, F., Pazos-Gil, M., Tamarit, J., Ros, J., and Cabiscol, E. (2024). Deciphering the ferroptosis pathways in dorsal root ganglia of Friedreich ataxia models. The role of LKB1/AMPK, KEAP1, and GSK3β in the impairment of the NRF2 response. Redox Biology *76*, 103339. https://doi.org/10.1016/j.redox.2024.103339.
20. Mincheva-Tasheva, S., Obis, E., Tamarit, J., and Ros, J. (2014). Apoptotic cell death and altered calcium homeostasis caused by frataxin depletion in dorsal root ganglia neurons can be prevented by BH4 domain of Bcl-xL protein. Human Molecular Genetics *23*, 1829–

1841. https://doi.org/10.1093/hmg/ddt576.
21. Yang, W., Thompson, B., Miellet, S., Maddock, M., Napierala, M., Dottori, M., and Kwa, F. (2025). Sulforaphane Targets Multiple Pathological Processes in Friedreich Ataxia Patient-Induced Pluripotent Stem Cell-Derived Sensory Neurons. Antioxid Redox Signal. https://doi.org/10.1089/ars.2024.0756.
22. Mazzara, P.G., Muggeo, S., Luoni, M., Massimino, L., Zaghi, M., Valverde, P.T.-T., Brusco, S., Marzi, M.J., Palma, C., Colasante, G., et al. (2020). Frataxin gene editing rescues Friedreich's ataxia pathology in dorsal root ganglia organoid-derived sensory neurons. Nat Commun *11*, 4178. https://doi.org/10.1038/s41467-020-17954-3.
23. Dionisi, C., Chazalon, M., Rai, M., Keime, C., Imbault, V., Communi, D., Puccio, H., Schiffmann, S.N., and Pandolfo, M. (2023). Proprioceptors-enriched neuronal cultures from induced pluripotent stem cells from Friedreich ataxia patients show altered transcriptomic and proteomic profiles, abnormal neurite extension, and impaired electrophysiological properties. Brain Communications *5*, fcad007. https://doi.org/10.1093/braincomms/fcad007.
24. Griso, O., and Puccio, H. (2020). Primary Cultures of Pure Embryonic Dorsal Root Ganglia Sensory Neurons as a New Cellular Model for Friedreich's Ataxia. In Trinucleotide Repeats: Methods and Protocols, G.-F. Richard, ed. (Springer New York), pp. 241–253. https://doi.org/10.1007/978-1-4939-9784-8_15.
25. Perdomini, M., Belbellaa, B., Monassier, L., Reutenauer, L., Messaddeq, N., Cartier, N., Crystal, R.G., Aubourg, P., and Puccio, H. (2014). Prevention and reversal of severe mitochondrial cardiomyopathy by gene therapy in a mouse model of Friedreich's ataxia. Nat. Med. *20*, 542–547. https://doi.org/10.1038/nm.3510.
26. Held, P. (2018). Using Phenol Red to Assess pH in Tissue Culture Media. In, pp. 1–13. https://www.biotek.com/resources/application-notes/using-phenol-red-to-assess-ph-in-tissue-culture-media/.
27. Guillon, B., Bulteau, A.-L., Wattenhofer-Donzé, M., Schmucker, S., Friguet, B., Puccio, H., Drapier, J.-C., and Bouton, C. (2009). Frataxin deficiency causes upregulation of mitochondrial Lon and ClpP proteases and severe loss of mitochondrial Fe-S proteins. FEBS J. *276*, 1036–1047. https://doi.org/10.1111/j.1742-4658.2008.06847.x.
28. Chaudhry, R., and Varacallo, M. (2020). Biochemistry, Glycolysis. In StatPearls (StatPearls Publishing).
29. TeSlaa, T., and Teitell, M.A. (2014). Techniques to Monitor Glycolysis. Methods Enzymol *542*, 91–114. https://doi.org/10.1016/B978-0-12-416618-9.00005-4.
30. Rouault, T.A., and Maio, N. (2017). Biogenesis and functions of mammalian iron-sulfur proteins in the regulation of iron homeostasis and pivotal metabolic pathways. J. Biol. Chem. *292*, 12744–12753. https://doi.org/10.1074/jbc.R117.789537.
31. Petrat, F., Weisheit, D., Lensen, M., de Groot, H., Sustmann, R., and Rauen, U. (2002). Selective determination of mitochondrial chelatable iron in viable cells with a new fluorescent sensor. Biochem. J. *362*, 137–147. https://doi.org/10.1042/0264-6021:3620137.
32. Cui, H., Kong, Y., and Zhang, H. (2011). Oxidative Stress, Mitochondrial Dysfunction, and Aging. Journal of Signal Transduction *2012*, 646354. https://doi.org/10.1155/2012/646354.
33. Morris, T.W., Reed, K.E., and Cronan, J.E. (1994). Identification of the gene encoding lipoate-protein ligase A of Escherichia coli. Molecular cloning and characterization of the lplA gene and gene product. J. Biol. Chem. *269*, 16091–16100.
34. Mihaylova, M.M., and Shaw, R.J. (2011). The AMP-activated protein kinase (AMPK) signaling pathway coordinates cell growth, autophagy, & metabolism. Nat Cell Biol *13*, 1016–1023. https://doi.org/10.1038/ncb2329.
35. Kim, J., and Guan, K.-L. (2019). mTOR as a central hub of nutrient signalling and cell growth. Nature Cell Biology *21*, 63–71. https://doi.org/10.1038/s41556-018-0205-1.

36. Al-Mahdawi, S., Pinto, R.M., Varshney, D., Lawrence, L., Lowrie, M.B., Hughes, S., Webster, Z., Blake, J., Cooper, J.M., King, R., et al. (2006). GAA repeat expansion mutation mouse models of Friedreich ataxia exhibit oxidative stress leading to progressive neuronal and cardiac pathology. Genomics *88*, 580–590. https://doi.org/10.1016/j.ygeno.2006.06.015.
37. Chandran, V., Gao, K., Swarup, V., Versano, R., Dong, H., Jordan, M.C., and Geschwind, D.H. (2017). Inducible and reversible phenotypes in a novel mouse model of Friedreich's Ataxia. eLife *6*. https://doi.org/10.7554/eLife.30054.
38. Mollá, B., Muñoz-Lasso, D.C., Riveiro, F., Bolinches-Amorós, A., Pallardó, F.V., Fernandez-Vilata, A., de la Iglesia-Vaya, M., Palau, F., and Gonzalez-Cabo, P. (2017). Reversible Axonal Dystrophy by Calcium Modulation in Frataxin-Deficient Sensory Neurons of YG8R Mice. Front Mol Neurosci *10*, 264. https://doi.org/10.3389/fnmol.2017.00264.
39. Simon, D., Seznec, H., Gansmuller, A., Carelle, N., Weber, P., Metzger, D., Rustin, P., Koenig, M., and Puccio, H. (2004). Friedreich Ataxia Mouse Models with Progressive Cerebellar and Sensory Ataxia Reveal Autophagic Neurodegeneration in Dorsal Root Ganglia. J. Neurosci. *24*, 1987–1995. https://doi.org/10.1523/JNEUROSCI.4549-03.2004.
40. Calmels, N., Seznec, H., Villa, P., Reutenauer, L., Hibert, M., Haiech, J., Rustin, P., Koenig, M., and Puccio, H. (2009). Limitations in a frataxin knockdown cell model for Friedreich ataxia in a high-throughput drug screen. BMC Neurology *9*, 46. https://doi.org/10.1186/1471-2377-9-46.
41. Cossée, M., Puccio, H., Gansmuller, A., Koutnikova, H., Dierich, A., LeMeur, M., Fischbeck, K., Dollé, P., and Kœnig, M. (2000). Inactivation of the Friedreich ataxia mouse gene leads to early embryonic lethality without iron accumulation. Hum. Mol. Genet. *9*, 1219–1226. https://doi.org/10.1093/hmg/9.8.1219.
42. Ben-Shimon, L., Paul, V.D., David-Kadoch, G., Volpe, M., Stümpfig, M., Bill, E., Mühlenhoff, U., Lill, R., and Ben-Aroya, S. (2018). Fe-S cluster coordination of the chromokinesin KIF4A alters its subcellular localization during mitosis. J. Cell. Sci. *131*. https://doi.org/10.1242/jcs.211433.
43. Baranovskiy, A.G., Siebler, H.M., Pavlov, Y.I., and Tahirov, T.H. (2018). Iron-Sulfur Clusters in DNA Polymerases and Primases of Eukaryotes. Methods Enzymol *599*, 1–20. https://doi.org/10.1016/bs.mie.2017.09.003.
44. Wu, S.-B., Wu, Y.-T., Wu, T.-P., and Wei, Y.-H. (2014). Role of AMPK-mediated adaptive responses in human cells with mitochondrial dysfunction to oxidative stress. Biochim. Biophys. Acta *1840*, 1331–1344. https://doi.org/10.1016/j.bbagen.2013.10.034.
45. Han, Y., Wang, Q., Song, P., Zhu, Y., and Zou, M.-H. (2010). Redox Regulation of the AMP-Activated Protein Kinase. PLOS ONE *5*, e15420. https://doi.org/10.1371/journal.pone.0015420.
46. Mackenzie, R.M., Salt, I.P., Miller, W.H., Logan, A., Ibrahim, H.A., Degasperi, A., Dymott, J.A., Hamilton, C.A., Murphy, M.P., Delles, C., et al. (2013). Mitochondrial reactive oxygen species enhance AMP-activated protein kinase activation in the endothelium of patients with coronary artery disease and diabetes. Clin Sci (Lond) *124*, 403–411. https://doi.org/10.1042/CS20120239.
47. Wu, S.-B., and Wei, Y.-H. (2012). AMPK-mediated increase of glycolysis as an adaptive response to oxidative stress in human cells: Implication of the cell survival in mitochondrial diseases. Biochimica et Biophysica Acta (BBA) - Molecular Basis of Disease *1822*, 233–247. https://doi.org/10.1016/j.bbadis.2011.09.014.
48. Gough, D.R., and Cotter, T.G. (2011). Hydrogen peroxide: a Jekyll and Hyde signalling molecule. Cell Death Dis *2*, e213–e213. https://doi.org/10.1038/cddis.2011.96.
49. Ristow, M., and Zarse, K. (2010). How increased oxidative stress promotes longevity and metabolic health: The concept of mitochondrial hormesis (mitohormesis). Experimental Gerontology *45*, 410–418. https://doi.org/10.1016/j.exger.2010.03.014.

50. Sid, B., Verrax, J., and Calderon, P.B. (2013). Role of AMPK activation in oxidative cell damage: Implications for alcohol-induced liver disease. Biochem Pharmacol *86*, 200–209. https://doi.org/10.1016/j.bcp.2013.05.007.
51. Thannickal, V.J., and Fanburg, B.L. (2000). Reactive oxygen species in cell signaling. American Journal of Physiology-Lung Cellular and Molecular Physiology *279*, L1005–L1028. https://doi.org/10.1152/ajplung.2000.279.6.L1005.
52. Qiu, X., Liu, K., Xiao, L., Jin, S., Dong, J., Teng, X., Guo, Q., Chen, Y., and Wu, Y. (2018). Alpha-lipoic acid regulates the autophagy of vascular smooth muscle cells in diabetes by elevating hydrogen sulfide level. Biochimica et Biophysica Acta (BBA) - Molecular Basis of Disease *1864*, 3723–3738. https://doi.org/10.1016/j.bbadis.2018.09.005.
53. Zhou, L., and Cheng, Y. (2019). Alpha-lipoic acid alleviated 6-OHDA-induced cell damage by inhibiting AMPK/mTOR mediated autophagy. Neuropharmacology *155*, 98–103. https://doi.org/10.1016/j.neuropharm.2019.04.009.
54. Dionisi, C., Rai, M., Chazalon, M., Schiffmann, S.N., and Pandolfo, M. (2020). Primary proprioceptive neurons from human induced pluripotent stem cells: a cell model for afferent ataxias. Sci Rep *10*, 7752. https://doi.org/10.1038/s41598-020-64831-6.

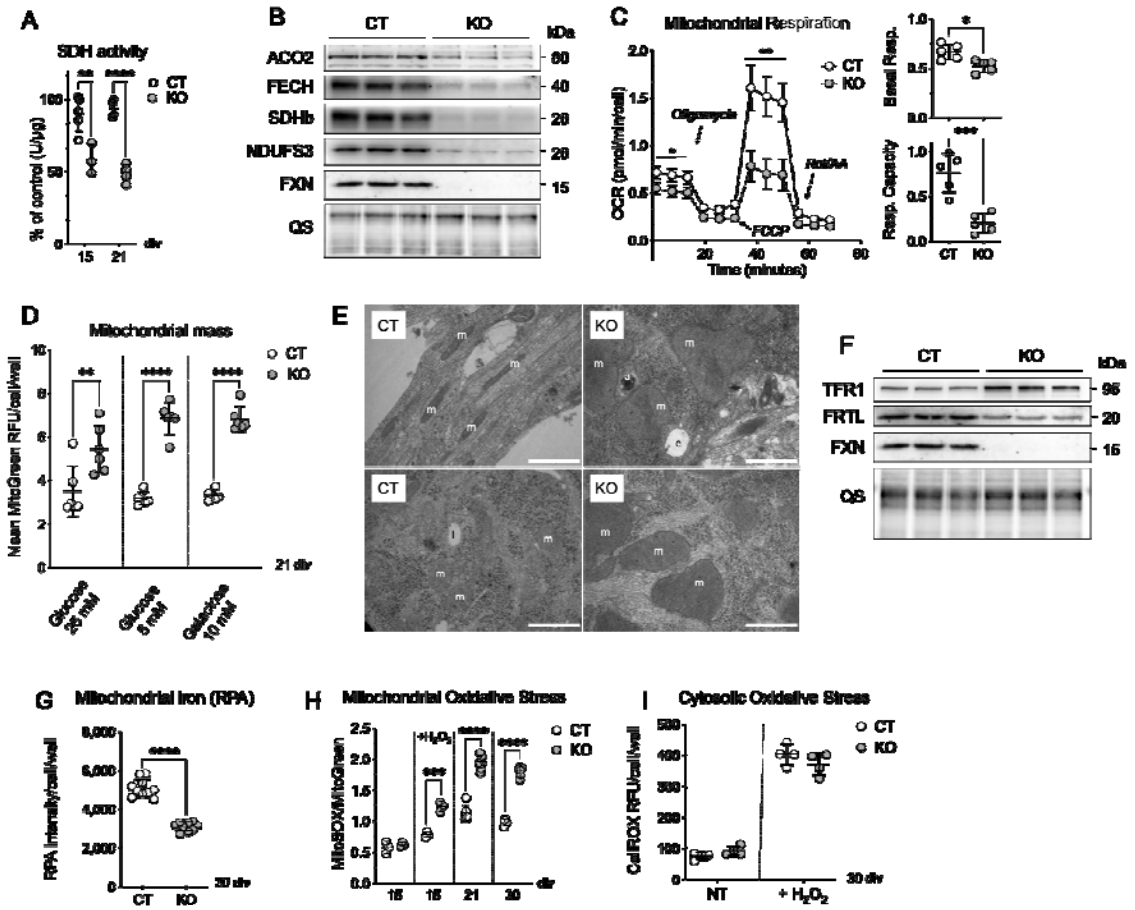

Figure 1: Sensory neurons depleted for FXN recapitulate several FA-associated biochemical and cellular pathological features *in vitro*.

(A) Spectrophotometric measurements of succinate dehydrogenase (SDH) enzymatic activity on sensory neurons at 15 and 21 div. n = 5 control and 3-4 KO cultures. (B) Levels of mitochondrial proteins containing Fe-S clusters at 21 div. ACO2 = Aconitase; FECH = ferrochelatase; SDHb = Succinate Dehydrogenase B (Complex II); NDUFS3 = Complex I; FXN = FXN; QS=QuickStain (total protein levels). (C) Oxygen Consumption Rate (OCR) was measured by Seahorse Analyzer at 15 div through addition of different respiratory chain inhibitors, as indicated. Rot/AA = Rotenone/Antimycin A. Right panels show quantifications for basal respiration and maximal respiration capacity. n = 5 cultures each group. (D) Total mitochondrial mass measured in sensory neurons at 21 div by Mitotracker Green fluorescent probe under different culture conditions. Dots indicate averaged RFU (Relative Fluorescence Units) values from every cell of one well (96-well plates, about 300 cells/well). (E) Representative electron microscopy images of CT and KO sensory neurons after 30 div. m, mitochondria; e, endosome; a, autophagosome; L, lipids. Scale bars: 1 µm. (F) Protein levels of iron metabolism related proteins, transferrin receptor 1 (TFR1) and ferritin light chain (FRTL) in CT and KO sensory neurons at 21 div. (G) Mitochondrial iron content measured at 30 div by RPA sensor. RPA signal is inversely correlated to mitochondrial iron levels. n = 9-10 wells. (H) Mitochondrial oxidative stress assessed by MitoSOX fluorescent probe in sensory neurons at 15, 21 and 30 div, and normalized to mitochondrial content by

Mitotracker Green FM. Cells at 15 div were treated with or without 10 µM H_2O_2. (I) Cytosolic oxidative stress assessed by CellROX. Fluorescent probe in sensory neurons at 30 div in DRG neurons, in the presence or absence of 10 µM H_2O_2 treatment. *p<0.05; **p<0.01; ***p<0.001; ****p<0.0001 (Student t-test). Error bars indicate SD.

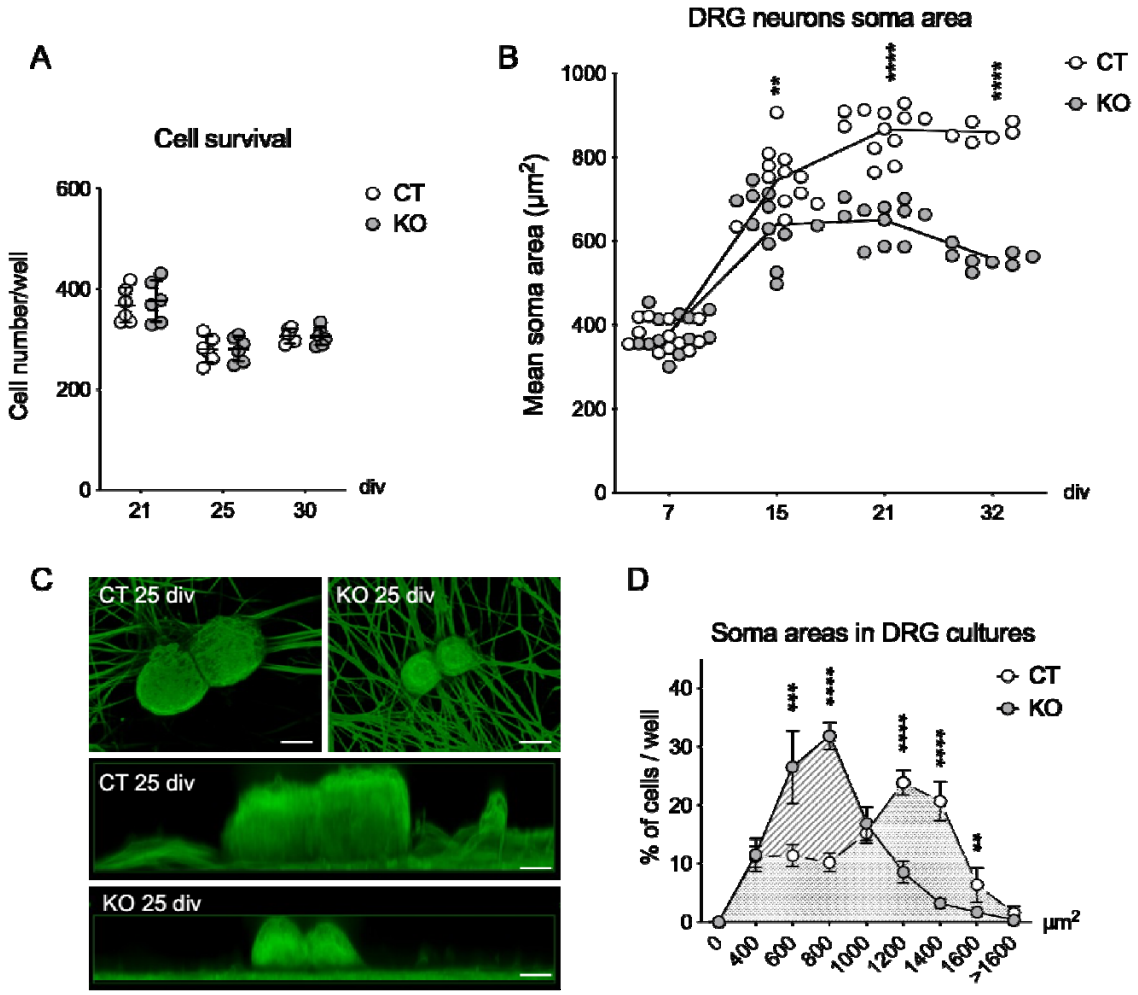

Figure 2: Sensory neurons present similar survival rate but decreased soma area in the absence of FXN.

(A) Cell count over time measured by Hoechst staining. n = 6 wells (B) Sensory neuron soma area measured by Hoechst staining (reflection of the signal throughout the cell body) at different time points. Dots indicate averaged areas from about 300 cells in one well (8-10 wells analyzed)). n = 6-12 independent cultures. (C) 3D representation of NF200-positive cells in CT and KO cultures at 25 div, acquired by z-scan with confocal microscopy. Scale bar = 10 µm. (D) Distribution frequency plots of soma areas in sensory neuron cultures. n = 6 wells (about 300 cells/well) at 25 div. (B, D) Two-way ANOVA with Geisser Greenhouse Correction; **p<0.01; ***p<0.001; ****p<0.0001. Error bars indicate SD.

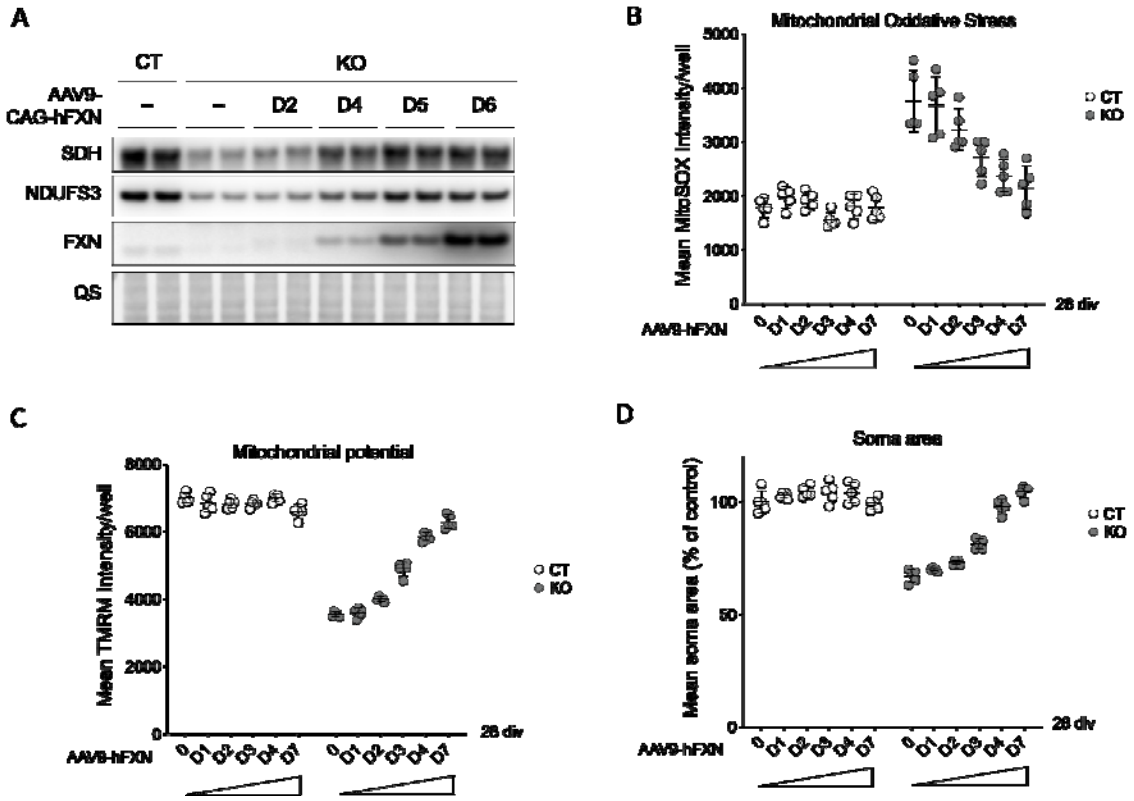

Figure 3: Dose-dependent reversal of phenotype in KO sensory neurons by exogenous hFXN expression.

Control (CT) and FXN-depleted (KO) sensory neurons were cultured for 7 div, infected with different concentrations of AAV-CAG-hFXN-HA viral particles. (A) Levels of the Fe-S containing proteins SDH and NDUFS3 in CT and KO sensory neuron cultures without or with increasing doses of AAV-CAG-hFXN-HA infection: 3.6 $x10^7$ vg/mL (D2) ; 1.8 $x10^8$ vg/mL (D4) ; 9 $x10^8$ vg/mL (D5) ; 4.5 $x10^9$ vg/mL (D6). Note, anti-FXN antibody (clone 4F9) has an extensively higher affinity for hFXN than mouse FXN (mFXN). (B) Mitochondrial oxidative stress assessed by MitoSOX signal following increase in hFXN expression. (C) Mitochondrial membrane potential measured by TMRM following increase in exogenous hFXN expression. (B, C). Dots indicate averaged RFU from every cell of one well (96-well plates, about 300 cells/well). n = 4 wells. (D) Measurements of sensory neuron soma area after increase in hFXN expression (28 div). Dots indicate averaged areas from every cell of one well (96-well plates, about 300 cells/well). n = 4 wells. Two-way ANOVA with Geisser Greenhouse Correction was applied in B, C and D. ***$p<0.001$; ****$p<0.0001$. Error bars indicate SD.

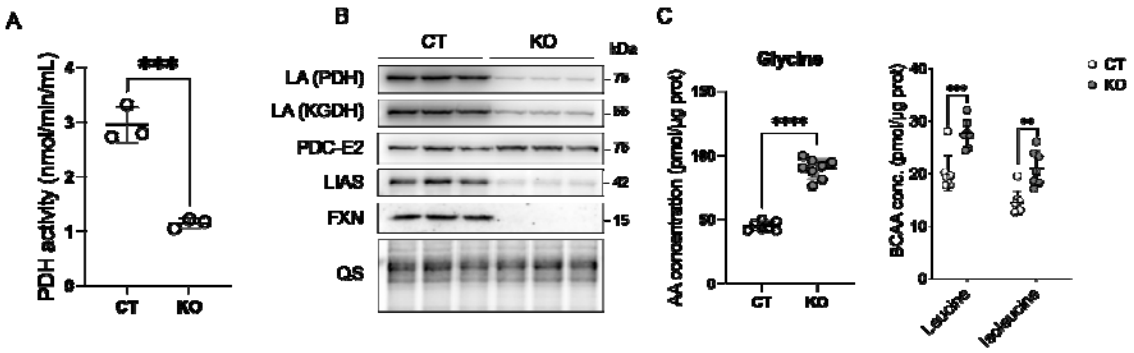

Figure 4: Lipoic acid-associated pathways are affected in frataxin deficient sensory neurons.

(A) PDH activity of CT and KO cells at 21 div. (B) Western Blot of Lipoic Acid (LA) on recipient enzymes PDH and KGDH, total PDC-E2, LIAS and FXN in CT and KO cells at 21 div. QS staining used as a loading control for quantification. (C) Measure of concentration of glycine, leucine and isoleucine in CT and KO cells at 30 div. (A, C) One-way ANOVA followed by Tukey for multiple comparison. *p<0.05; **p<0.01; ***p<0.001; ****p<0.0001. Error bars indicate SD.

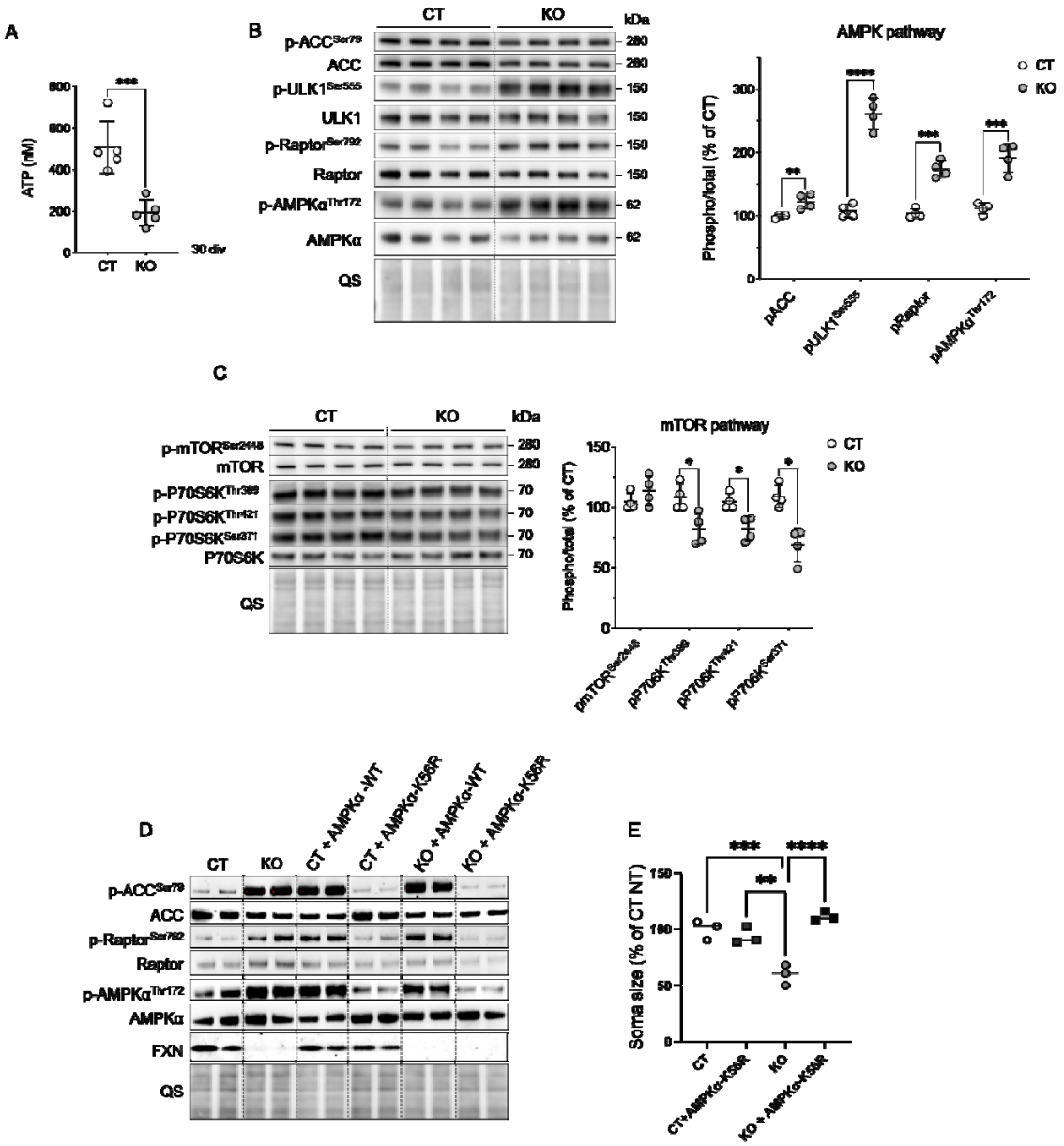

Figure 5: Activation and Rescue of AMPK/mTOR pathways in sensory neurons depleted for FXN

(A) ATP content in CT and KO sensory neurons at 30 div. (B) Western blot analysis of AMPK pathway in CT and KO cells. Right panel indicates quantification of the Western Blot. QS staining used as a loading control for quantification. (C) Western Blot analysis of the mTOR pathway. Right panel indicates quantification of the Western Blot. QS staining used as a loading control for quantification. (D) Western blot analysis of AMPK pathway in CT and KO cells with or without overexpression of a dominant-negative AMPKα mutant (AMPKα^{K56R}) or AMPKα WT. (E) DRG neuron soma area measured in CT and KO cells with or without AMPKα^{K56R} expression. Areas are expressed in percentage of averaged CT. *p<0.05; **p<0.01; ***p<0.001; ****p<0.0001. Error bars indicate SD. Student t-test was applied in A, B, C and one-way ANOVA followed by Tukey for multiple comparison was used in E.

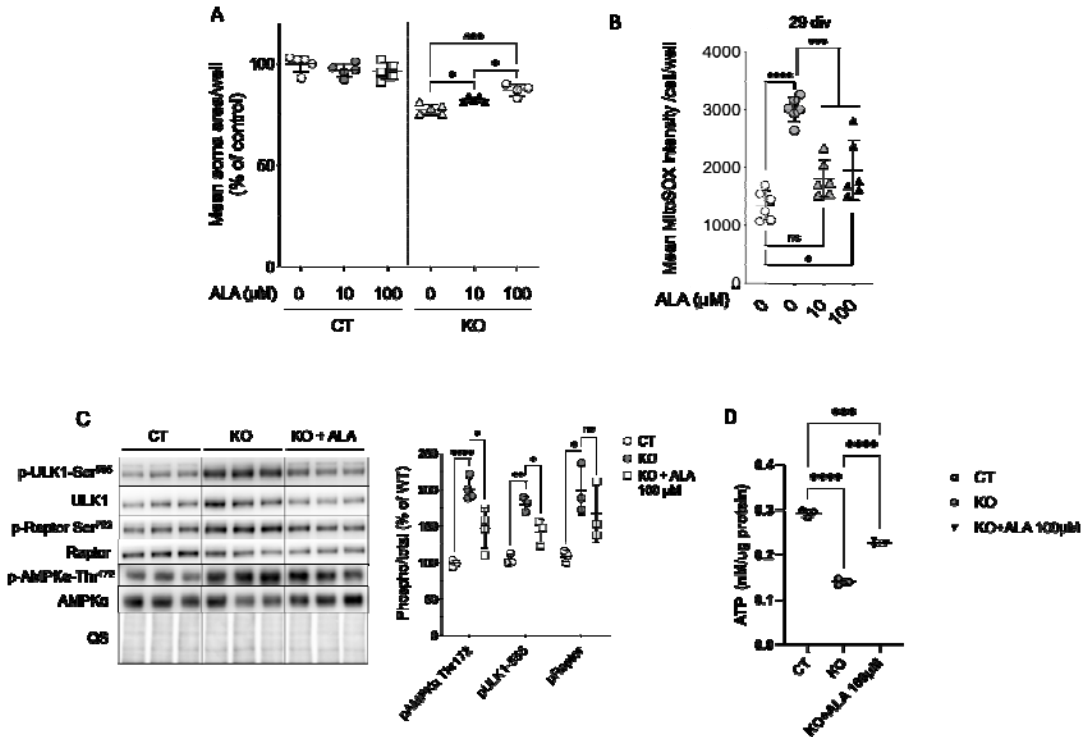

Figure 6: Antioxidant properties of ALA contribute to phenotypic rescue and prevents AMPK activation in frataxin-deficient neurons

(A) DRG neuron soma area measured in 96-well plates at 21 div, following ALA treatment. Dots indicate averaged areas from every cell of one well (96-well plates, about 300 cells/well). n = 4-5 wells. (B) Mitochondrial oxidative stress assessed by MitoSOX. MitoSOX fluorescence was acquired at 29 div in DRG CT or KO neurons treated with ALA. Dots indicate averaged values from every cell of one well (96-well plates, about 300 cells/well). (C) Western Blot of phosphorylated and total proteins of AMPK pathway, In CT or KO neurons treated with ALA (100 µM). Right panel indicates quantification of the Western Blot. QS staining used as a loading control for quantification. (D) ATP content in CT and KO sensory neurons treated or not with ALA at 30 div. (A-D) One-way ANOVA followed by Tukey for multiple comparison. *p<0.05; **p<0.01; ***p<0.001; ****p<0.0001. Error bars indicate SD.

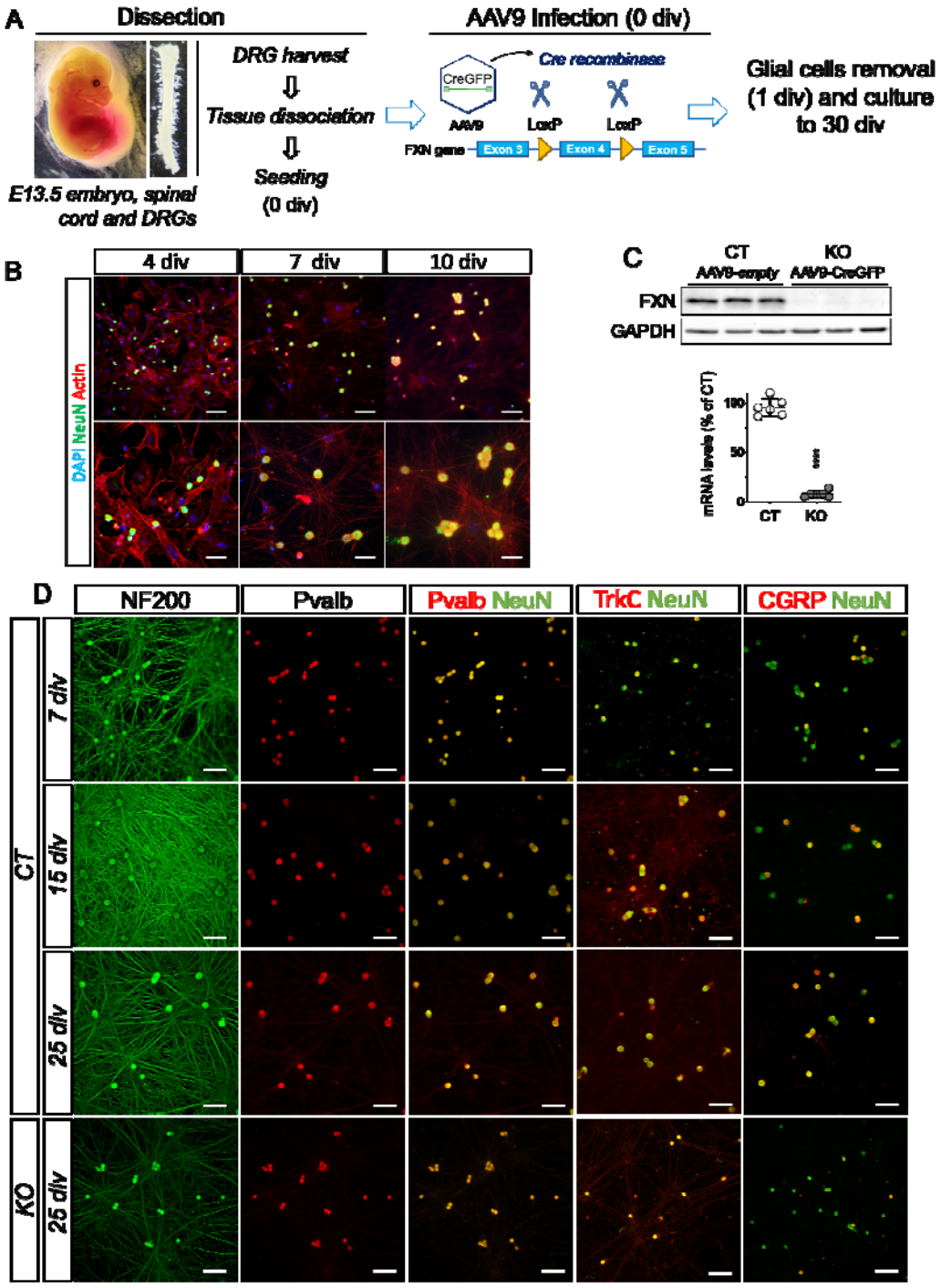
A
Dissection
AAV9 Infection (0 div)
E13.5 embryo, spinal cord and DRGs
DRG harvest
Tissue dissociation
Seeding (0 div)
CreGFP
AAV9
Cre recombinase
LoxP
LoxP
FXN gene
Exon 3
Exon 4
Exon 5
Glial cells removal (1 div) and culture to 30 div
B
4 div
7 div
10 div
DAPI NeuN Actin
C
CT
KO
AAV9-empty
AAV9-CreGFP
FXN
GAPDH
mRNA levels (% of CT)
100
50
0
CT
KO
D
NF200
Pvalb
Pvalb NeuN
TrkC NeuN
CGRP NeuN
CT
KO
7 div
15 div
25 div
25 div

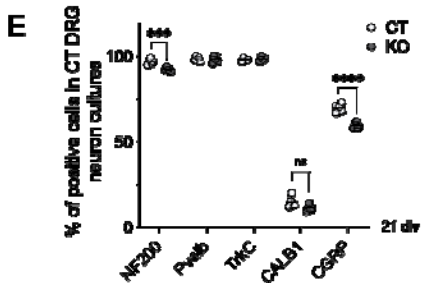
E
% of positive cells in CT DRG neuron cultures
100
50
0
CT
KO
21 div
NF200
Pvalb
TrkC
CALB1
CGRP

Figure S1:

(A) Summary steps of DRG sensory neuron culture model used for these studies. (B) Labeling of nuclei (DAPI), cytoskeleton (filamentous actin) (Phalloidin) and sensory neurons (NeuN) overtime in culture. Glial cells are removed from the culture following antimitotic agent treatment. Scale bars: 100 µm. (C) FXN protein levels (top) and gene expression (bottom) are depleted in AAV9-CreGFP infected cultures (KO), compared to AAV9-empty (control, CT) cultures after 15 div. (D) Sensory neurons fluorescently labeled at 7, 15, and 25 div with antibodies against neurofilament heavy (NF200), parvalbumine (Pvalb), Tropomyosin receptor kinase C (TrkC), calcitonin gene related peptide (CGRP) or pan-neuronal marker NeuN. At Scale bars: 100 µm. (E) Percentage of CT and KO cells positive for NF200, Pvalb, TrkC, CALB1 or CGRP at 21 div. *p<0.05; ****p<0.0001 (Student t-test). Error bars indicate SD.

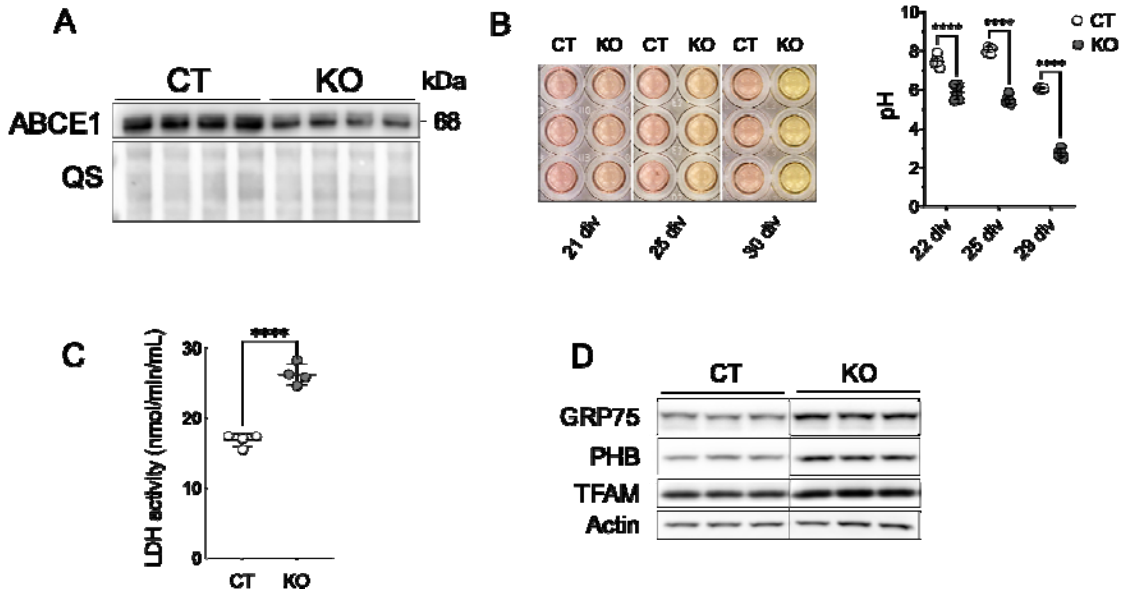

Figure S2

(A) Protein levels of ABCE1 (a cytosolic Fe-S protein) assayed by Western Blot in Control (CT) and FXN-depleted (KO) sensory neuron cultures after 21 div. (B) Color and pH quantification of culture media from CT and KO sensory neurons at 21, 25 and 30 div. (C) Lactate Dehydrogenase B (LDHb) activity at 25 div. n = 4. (D) Western Blot of mitochondrial markers Glucose-regulated protein 75 (GRP75), Prohibitin (Phb) and Transcription Factor A Mitochondrial (TFAM) at 30 div. Actin was used as a loading control. (B, C) Student t-test. ns = non-significant; **p<0.01; ***p<0.001; ****p<0.0001. Error bars indicate SD.

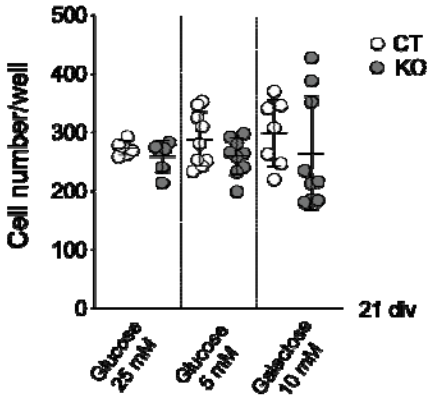

Figure S3

Total mitochondrial mass measured at 21 div by Mitotracker Green FM. Dots indicate averaged RFU (relative fluorescence units) values from every cell of one well (96-well plates, about 300 cells/well). Cells were treated with glycolysis inhibitory conditions from 7 div (5 mM glucose, 10 mM galactose). Student t-test. ns = non-significant; **p<0.01; ***p<0.001; ****p<0.0001. Error bars indicate SD.

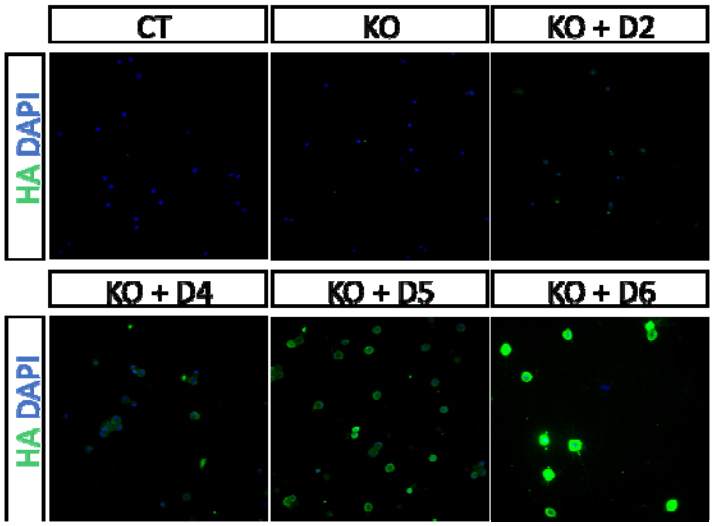

Figure S4

Control (CT) and FXN-depleted (KO) sensory neurons were cultured for 7 div, infected with different concentrations of AAV-CAG-hFXN-HA viral particles. (A) Detection of HA-tagged human FXN by immunofluorescence after increasing doses of AAV-CAG-hFXN-HA infection: 3.6 x10^7 vg/mL (D2) ; 1.8 x10^8 vg/mL (D4) ; 9 x10^8 vg/mL (D5) ; 4.5 x10^9 vg/mL (D6).

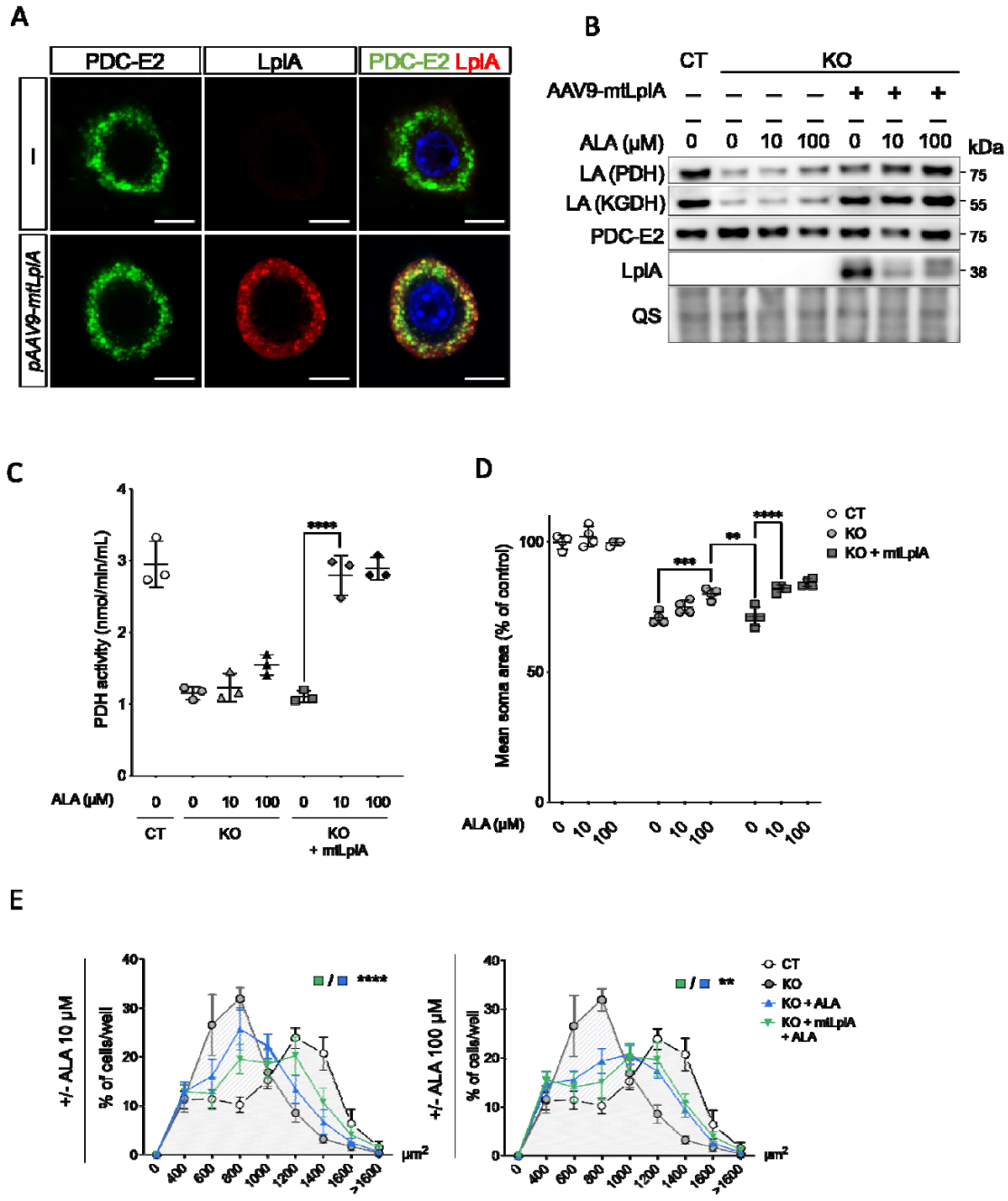

Figure S5

(A) Immunofluorescence against LplA (red) and co-localisation with mitochondrial marker PDC-E2 (green), in KO neurons infected with AAV9-mtLplA. Cells were further stained with DAPI (blue). Scale bar = 5 µm. (B) Western Blot of Lipoic Acid (LA) on recipient enzymes PDH and KGDH, total PDC-E2, LIAS and FXN at 21 div in CT or KO cells further infected with AAV9-mtLplA and treated by ALA. (C) PDH activity at 21 div of CT and KO neurons infected with AAV9-mtLplA and following alpha-Lipoic Acid (ALA) treatment. (D) DRG neuron soma area in CT, KO or KO + AAV9-mtLplA, measured in 96-well plates when treated with different ALA concentrations. Dots indicate averaged areas from every cell of one well (96-well plates, about 300 cells/well). n = 4 wells. (E) Cells ranked at 25 div by soma areas and

frequency of each group calculated (% of cells between N and N-1 size value) in CT and KO neurons infected with AAV9-mtLplA and following alpha-Lipoic Acid (ALA) treatment. n = 6 wells (about 300 cells/well). (B-C) One-way ANOVA followed by Tukey for multiple comparison. (D) Two-way ANOVA with Geisser Greenhouse Correction. *p<0.05; **p<0.01; ***p<0.001; ****p<0.0001. Error bars indicate SD.

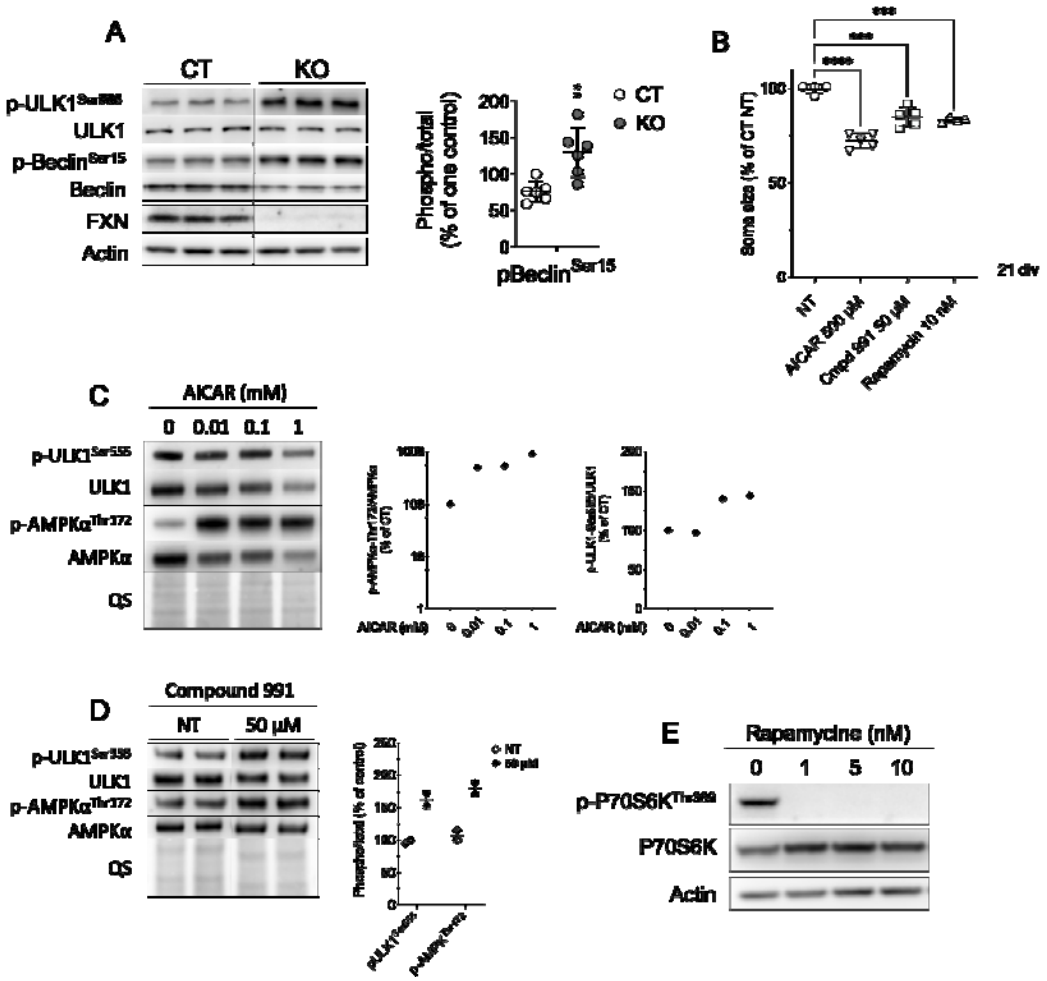

Figure S6

(A) Western Blot of ULK1, Beclin and phosphorylated residues at Serine 555 and Serine 15, respectively. Right panel shows quantification of phospho-Beclin^{Ser15} relative to total Beclin. Actin was used as a loading control for quantifications. Student t-test. **p<0.01. Error bars indicate SD. (B) Measurement of soma size in 21 div CT cultures untreated (NT) or treated for 14 days with 500 µM AICAR, 50 µM Compound 991 or 10 nM Rapamycin. n = 5-10 wells (about 300 cells/well). One-way ANOVA followed by Tukey for multiple comparison; ****p<0.0001. Error bars indicate SD. (C, D) Western Blot of phosphorylated and total proteins of AMPK pathway at 21 div following 96h treatment with different concentrations of AICAR (C) or 50 µM Compound 991 (D). Right panels indicate quantification of the Western Blot. QS staining was used as a loading control for quantifications. (E) Western Blot of phosphorylated and total proteins of mTOR pathway, following 96h treatment with different concentrations of rapamycin. Actin was used as a loading control.

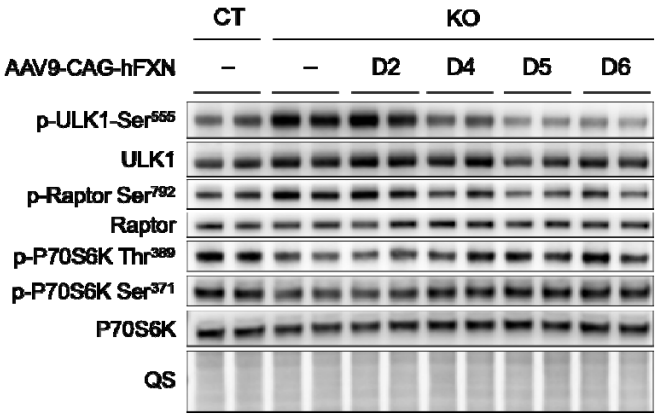

Figure S7

Western blot analysis of phosphorylated and total proteins of AMPK and mTOR downstream targets, after increasing doses of AAV-CAG-hFXN-HA infection: 3.6 x10^7 vg/mL (D2) ; 1.8 x10^8 vg/mL (D4) ; 9 x10^8 vg/mL (D5) ; 4.5 x10^9 vg/mL (D6).

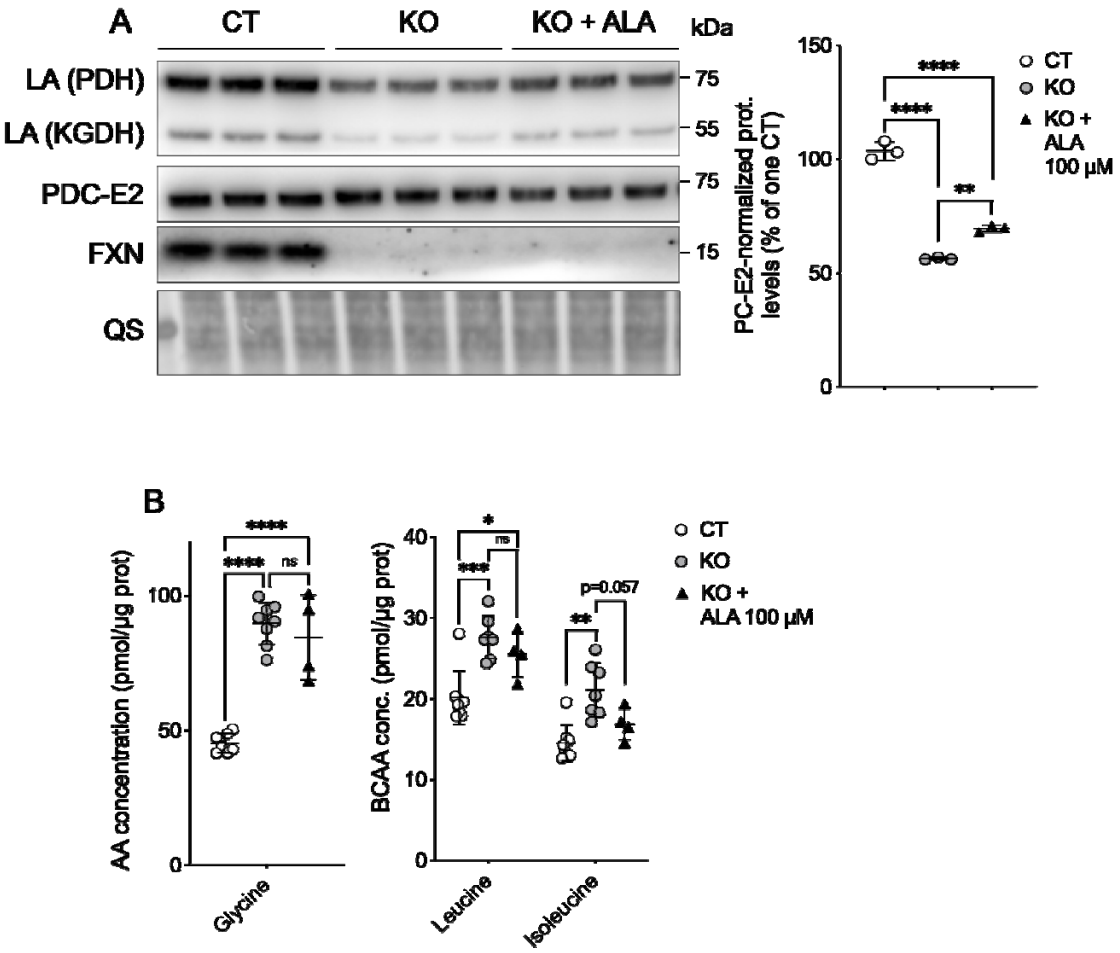

Figure S8

(A) Western Blot of Lipoic Acid (LA) on recipient enzymes PDH and KGDH, total PDC-E2 and FXN at 21 div. QS staining used as a loading control for quantification. (B) Measure of concentration of glycine,

leucine and isoleucine in CT and KO cells at 30 div, with or without ALA treatment. One-way ANOVA followed by Tukey for multiple comparison. *$p<0.05$; **$p<0.01$; ***$p<0.001$; ****$p<0.0001$. Error bars indicate SD.

Table S1

Antibody	Reference	Dilution
CALB1	C9848, Merck	1/2000
CGRP	24112, Immunostar	1/1000
HA	ab130275, Abcam	1/1000
NeuN	266 004, Synaptic Systems	1/500
NF200	ab4680, Abcam	1/1000
Pvalb	PV 27, Swant	1/2000
TrkC	AF1404, R&D Systems	1/500

Table S2

Antibody	Reference	Dilution
ABCE1	ab32270, Abcam	1/1000
ACC	3676, CST	1/2000
ACO2	R2377-IGBMC, Home made	1/2000
Actin	3700, CST	1/1000
AMPKα	5831, CST	1/2000
Beclin	3495, CST	1/1000
FECH	R2381-IGBMC, Home made	1/2000
FRTL	ab69090, Abcam	1/1000
FXN	Clone 4F9, Home made	1/5000
GAPDH	MAB374, Merck	1/40.000
GRP75	sc-133137, SCBT	1/1000
LA	437695, Calbiochem	1/5000
LIAS	ab96302, Abcam	1/1000
LplA	orb51462, Biorbyt	1/1000
mTOR	2983, CST	1/1000
NDUFS3	439200, Invitrogen	1/2000
p-ACC^{Ser79}	11818, CST	1/2000
p-AMPKα^{Ser485}	4185, CST	1/1000
p-AMPKα^{Thr172}	50081, CST	1/1000
p-Beclin^{Ser15}	13825, CST	1/1000
PDC-E2	sc-271352, SCBT	1/2000
p-mTOR^{Ser2448}	5536, CST	1/1000
p-P70S6K^{Ser371}	9208, CST	1/500
p-P70S6K^{Thr389}	9234, CST	1/500
p-P70S6K^{Thr421}	9204, CST	1/1000
p-Raptor^{Ser792}	2083, CST	1/1000
p-ULK1^{Ser555}	5869, CST	1/1000
P70S6K	9202, CST	1/2000
Phb	ab28172, Abcam	1/1000
Raptor	2280, CST	1/1000
SDH	ab14714, Abcam	1/2000
TFAM	ab131607, Abcam	1/1000
TFR1	ab84036, Abcam	1/2000
ULK1	8054, CST	1/1000

Table S3

Gene	Fd-Primer	Rv-Primer
Cycs	GAACGTTCGTGGTGTTGACC	CCCAGGTGATGCCTTTGTTCT
Fxn	ATGGCGTGCTCACCATTAAG	GGCCAATGAAGACAAGTCCA
Gapdh	GTGGACCTGACCTGCCGTCT	CTGTAGCCAAATTCGTTGTC
Grp75	GACAAGGATGCCCAAGGTTC	GGTAAAGACGCCTCCCAGAG
Nrf1	ATGTCCGCACAGAAGAGCAA	TGTACCAACCTGGATGAGCG
Pgc1a	GCAGGTCGAACGAAACTGAC	CTTGCTCTTGGTGGAAGCAG
Sdhb	TGGTGGAACGGAGACAAGTA	TGGCAGCGGTAGACAGAGAA
Tfam	ATAGGCACCGTATTGCGTGA	AGTTTTGCATCTGGGTGTTTAGC
Tom20	TGGGCTTTCCAAGTTACCTGA	TGGTCCACACCCTTCTCGTA
Vdac2	CTGTGTACCGGTATGCCCAC	GAAAATTCCACACCGCTGCAT